DE-FG02-97ER41022

FLORIDA STATE UNIVERSITY

HIGH ENERGY PHYSICS LABORATORY, Tallahassee, Florida 32306-3016

Direct Photon Plus One and Two Jet(s) Production in Proton-Antiproton Collisions at a Center of Mass Energy of 1.8 TEV

by
Christopher D. Shaffer

A dissertation submitted to the Department of Physics in partial fulfillment of the requirements for the degree of Doctor of Philosophy

August 1997

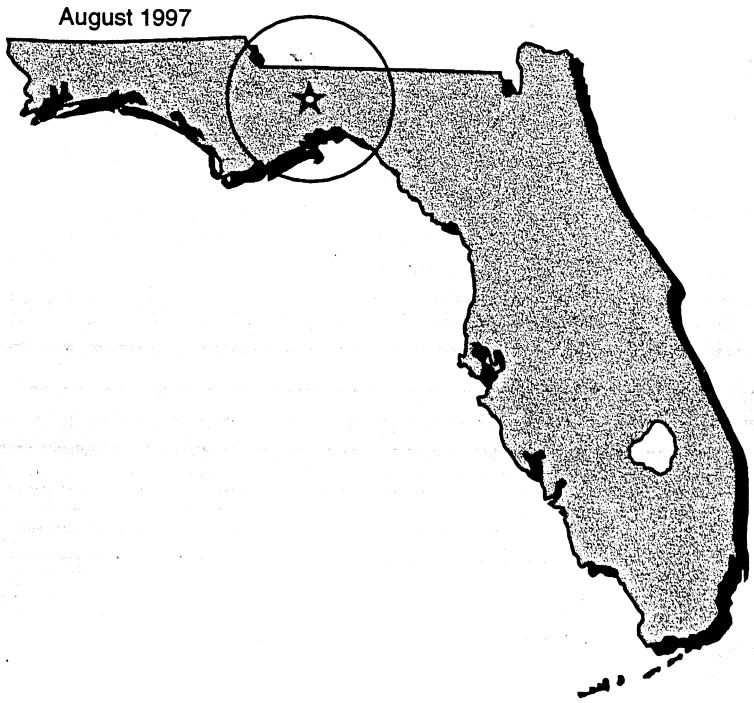

THE FLORIDA STATE UNIVERSITY
COLLEGE OF ARTS AND SCIENCES

DIRECT PHOTON PLUS ONE AND TWO JET(S) PRODUCTION IN PROTON-ANTIPROTON COLLISIONS AT A CENTER OF MASS ENERGY OF 1.8 TEV

By

CHRISTOPHER D. SHAFFER

A dissertation submitted to the
Department of Physics
in partial fulfillment of the
requirements for the degree of
Doctor of Philosophy

Degree Awarded:
Summer Semester, 1997

The members of the Committee approve the dissertation of Christopher D. Shaffer defended on April 8, 1997.

Vasken Hagopian

Vasken Hagopian
Professor Co-Directing dissertation

Stephan L. Linn
Professor Co-Directing dissertation

Joseph B. Schlenoff
Outside Committee Member

Paul Cottle
Committee Member

Joseph F. Owens III
Committee Member

To my parents, a down payment on an irrepayable debt.

DIRECT PHOTON PLUS ONE AND TWO JET(S) PRODUCTION IN PROTON-ANTIPROTON COLLISIONS AT A CENTER OF MASS ENERGY OF 1.8 TEV

Christopher D. Shaffer, Ph.D.
Florida State University, 1997
Major Professors: Vasken Hagopian, Ph.D. and Stephan L. Linn, Ph.D.

The cross sections for direct photon plus one and two jet(s) production in proton - antiproton collisions at a center of mass energy of 1.8 TeV have been measured for photons with pseudorapidity less than 0.9, and transverse energies between 20 and 100 GeV. The photon plus one jet cross section is in good agreement with the theoretical predictions of the next to leading order Standard Model calculations for jets with transverse energies greater than 25 GeV. The photon plus two jets cross section is in good agreement with the leading order theoretical prediction for events that have jets between 25 and 65 GeV of transverse energy.

ACKNOWLEDGEMENTS

Many people have assisted me in my tenure as a graduate student and in the completion of this work. The first is Vasken Hagopian, who got me into High Energy, and has seen me through good times and bad with consistent care and support over the last seven years. Thank you for the faith and support that you have always shown me. My thesis co-advisor, Stephan Linn, has mentored, constructively criticized, and vastly improved my work, and I owe much of my improvement as a natural philosopher to the countless hours he has spent with me explaining how things work, and how science should be done. In the same breath, both Steve Linn and Islara Souto have been wonderful and supportive friends (and family) over the last few years. My sanity, and what little natural good humor I have, are both intact due to the warmth you've shown and happiness you've given me, not to mention the many (delicious!) meals that have kept body and soul together!

The faculty of the High Energy group have always taken the time to give thoughtful and enlightening answers to my questions, no matter how mundane or bizarre. Many thanks are due to Harrison Prosper for introducing me to the correct way to do statistical analysis, even if I didn't get to use it in this analysis. You have successfully 'corrupted' the youth in my case! Joseph Owens and Howard Baer have both been great sources of information on the theoretical aspects of HEP, especially when the theoretical literature proved impenetrable to my experimentalist's thinking.

All of my colleagues on the DØ experiment have always shown a great willingness to give of their time and expertise, but I've pestered some more than others, so I'll try to give them the extra credit they deserve. Amber Boehnlein, for always taking time to guide me through the intricacies of DØ software, particularly Trigsim, no matter how busy your schedule. To Paul Russo, for great assistance in making the temperamental FNALD0 cluster work, and for shared humor. To my photon colleagues past and present, particularly Robert Madden, Salvatore Fahey, Paul Rubinov, and Steve Jerger, thanks for many illuminating conversations, and of course, all the cooperation and teamwork that it has taken to produce good physics

results. Thanks also go to Tacy Joffe-Minor for good natured help with a variety of problems unique to boson plus jet studies.

To my many friends that have given me solace and occasion to laugh, especially at myself, I give my special thanks. Willi, for listening to me grousing, Paul for 'growth experiences', S.B.M. for playing the diamond to my emerald, M.S. for sage advise and great company

Finally I'd like to thank my parents and grandparents for their lifetime of unswerving support. I love you more each year.

CONTENTS

LIST OF TABLES viii

LIST OF FIGURES x

1 Introduction 1

1.1 Quantum Chromodynamics 1

1.2 Some Previous Direct Photon Measurements 6

1.3 The Dissertation 10

2 The DØ Detector 11

2.1 Tracking in DØ 11

2.2 Calorimetry in DØ 13

2.3 Triggering in DØ 15

2.3.1 Level 0 15

2.3.2 Level 1 16

2.3.3 Level 2 16

2.4 Event Reconstruction 17

3 The Isolated Photon + Jet(s) Cross Sections 22

3.1 The Cross Sections $\sigma_{\gamma+Jet}$ and $\sigma_{\gamma+2Jets}$ 22

3.2 Data Sample 22

3.3 Fiducial Cuts 24

3.4 The Kinematic Region 25

3.5 Missing E_T Cut 25

3.6 Jet Cuts 25

3.7 Photon Candidate Selection Cuts 27
3.7.1 Charged Track Cut 29
3.8 Photon Background Subtraction 32

4 Monte Carlo **37**
4.1 Event Generation 37
4.2 Detector Simulation 38
4.3 Noise and Pileup Effects 39
4.4 Comparison of Monte Carlo and Data 39

5 Comparison of Theory and Data **42**
5.1 Theoretical Calculations 42
5.2 The Measured Exclusive Isolated Photon Cross Sections 47
5.2.1 Errors on the Measurement 52
5.2.2 Uncertainty Due to Jet Energy Scale 54

6 Summary and Conclusions **56**

A The Systematic Dependance of the Cross Section Measurements on the Photon Candidate Selection Cuts **58**

B Plots **63**
B.1 Trigger Efficiencies as a Function of E_T^γ 63
B.2 Purity Fits 65

BIBLIOGRAPHY **69**

LIST OF TABLES

3.1 Initial Data Sample 23

3.2 Z Vertex Cut Efficiency from Data 24

3.3 Charged Track Cut Efficiencies 29

4.1 $W \rightarrow e\nu$ Distribution Centroids for Data and Monte Carlo 40

5.1 Photon Candidate Selection Cut Variations 53

5.2 Summary Table of Cross Section Parameters for $\sigma_{\gamma+jet}$. 55

5.3 Summary Table of Cross Section Parameters for $\sigma_{\gamma+2jets}$. 55

6.1 Table of $\chi^2/d.o.f.$ for Each Differential Cross Section 57

LIST OF FIGURES

1.1 A Sketch of a $p\overline{p}$ Interaction 3

1.2 A Selection of Feynman Diagrams 4

2.1 The DØCalorimeter and Tracking Chambers 21

3.1 Data Based Estimate of the missing E_T cut efficiency ϵ_m. 26

3.2 Standard Jet Cuts 28

3.3 Photon Candidate Selection Cut Efficiency as Determined from MC Photons as a Function of E_T^γ 30

3.4 Photon Selection Cuts 31

3.5 Discriminant Variable of Data, MC Photons and MC Jets 33

3.6 Fit of MC to Data 35

3.7 Measured Photon Candidate Purity as a Function of E_T^γ 36

4.1 Distributions of the discriminant variable, the isolation E_T, the cluster electromagnetic fraction and the shower shape variable χ^2 for Data and MC Electrons from W$\rightarrow e + \bar{\nu}_e$ events. 41

5.1 Dependance of the Differential Cross Sections on $Q^2 = (0.5\,, 1.0\,, 2.0)E_T^2$ 46

5.2 The Differential Cross Sections $\frac{d\sigma_{\gamma+jet}}{dE_T^\gamma}$ and $\frac{d\sigma_{\gamma+2jets}}{dE_T^\gamma}$ given $E_T^{jet(s)} > 25$ through 75 GeV. 49

5.3 The Differential Cross Sections $\frac{d\sigma_{\gamma+jet}}{dE_T^\gamma}$ and $\frac{d\sigma_{\gamma+2jets}}{dE_T^\gamma}$ given $E_T^{jet(s)} > 25$ through 75 GeV plotted in (data-theory)/theory form. 50

5.4 The Differential Cross Sections $\frac{d\sigma_{\gamma+jet}}{dE_T^\gamma}$ and $\frac{d\sigma_{\gamma+2jets}}{dE_T^\gamma}$ given $E_T^{jet(s)} > 25$ GeV plotted in (data-theory)/theory form. 51

A.1 Dependance of the Cross Sections on the Electromagnetic Fraction Cut 59
A.2 Dependance of the Cross Sections on the Shower Shape Cut 60
A.3 Dependance of the Cross Sections on the Isolation Cut 61
A.4 Dependance of the Cross Sections on the Jet Energy Scale 62

B.1 Turnon of All Triggers 64
B.2 Fitted Distributions of the Discriminant Variable 66
B.3 Fitted Distributions of the Discriminant Variable 67
B.4 Fitted Distributions of the Discriminant Variable 68

ABSTRACT

The cross sections for direct photon plus one and two jet(s) production in proton - antiproton collisions at a center of mass energy of 1.8 TeV have been measured for photons with pseudorapidity less than 0.9, and transverse energies between 20 and 100 GeV. The photon plus one jet cross section is in good agreement with the theoretical predictions of the next to leading order Standard Model calculations for jets with transverse energies greater than 25 GeV. The photon plus two jets cross section is in good agreement with the leading order theoretical prediction for events that have jets between 25 and 65 GeV of transverse energy.

CHAPTER 1
INTRODUCTION

1.1 Quantum Chromodynamics

Quantum Chromodynamics (QCD) is a theory derived to describe the behavior of the hadronic constituents (the quarks and gluons, collectively called partons) when they interact. For processes involving large momentum transfers, it does this by relating an observable high energy cross section to a perturbatively calculable parton level cross section through parton distribution functions [1]. Figure 1.1 is a representation of a proton anti-proton collision which resulted in the production of a direct photon and a spray of hadrons collectively called a jet. The two circles on the left represent the incoming proton and anti-proton. The lines labeled 'a' and 'b' represent partons which each received fractions (a/A) and (b/B) of their respective parent proton and anti-proton's momentum when they underwent the perturbatively calculable hard scattering represented by the circle in the center. The outgoing direct photon 'γ' and parton 'c' are then the immediate final state of the perturbative interaction. Parton 'c' then undergoes a process called hadronization and turns into a final state jet, the energy and position of which are experimentally measured. Note that the direct photon is produced in the perturbative interaction, not by the decay of a particle in a jet. The direct photon plus one jet cross section (σ) is given by a convolution of the parton level cross section and two parton distribution functions

$$\frac{d\sigma(p\bar{p} \rightarrow \gamma + jet)}{dx_a dx_b d\cos\theta^*} = \sum_{a,b} G_{a/A}(x_a) \times \hat{\sigma}(ab \rightarrow \gamma c) \times G_{b/B}(x_b)$$

where x_a and x_b are the fraction of the proton and antiproton's momenta carried by partons a and b respectively, θ^* is the parton level polar angle at which the photon

is emitted, $\hat{\sigma}(ab \rightarrow \gamma c)$ is the partonic cross section (calculated using perturbation theory for the energies discussed in this dissertation), and $G_{v/V}(x_v)$ are the parton distribution functions.

The perturbative part of the cross section is calculated by using appropriate combinations of the Feynman amplitudes from processes which yield the final state in question. Feynman amplitudes are momentum space analogs of the wavefunction overlap integrals from classical quantum mechanics, which when squared yield (for instance) atomic transition probabilities. The Feynman diagrams, examples of which are shown in figure 1.2, are graphical interpretations of the Feynman amplitudes. The diagrams in 'A' and 'B' show the leading order (LO) annihilation and Compton scattering processes respectively. Leading order means that the diagrams represent the first term in the perturbative expansion of the entire direct photon cross section. The diagrams in 'C' and 'D' show some of the tree level $2 \rightarrow 3$ processes. The term 'tree level' is used because the various lines in the diagrams branch out but never intersect. In 'E' are shown some of the one loop corrections to the $2 \rightarrow 2$ processes. These are the Compton and annihilation processes with the next to leading order (NLO) correction. All the processes shown (with many more like them) contribute to the full NLO calculation of the photon plus one jet cross section as will be discussed in chapter 5. The processes in 'C' and 'D' (and more like them) contribute to the photon plus two jet cross section at first order.

The parton distribution functions (pdf) are obtained from fits to cross section data (σ_{meas}) taken at multiple experiments, each in convolution with the appropriate choice of parton level cross section $\hat{\sigma}$. The pdf are theoretical constructs that depend explicitly upon the parton level cross sections from each process that is considered in the fit. Using cross section data from lepton on hadron ($e^{\pm}N$[1] ,$\mu^{\pm}N$,$\nu_{e,\mu}N$), hadron on hadron ($p\bar{p}$,pp,pN), and meson on nucleon ($\pi^{-}N$) collisions, the pdf for quarks

[1] N can be a proton or nucleon.

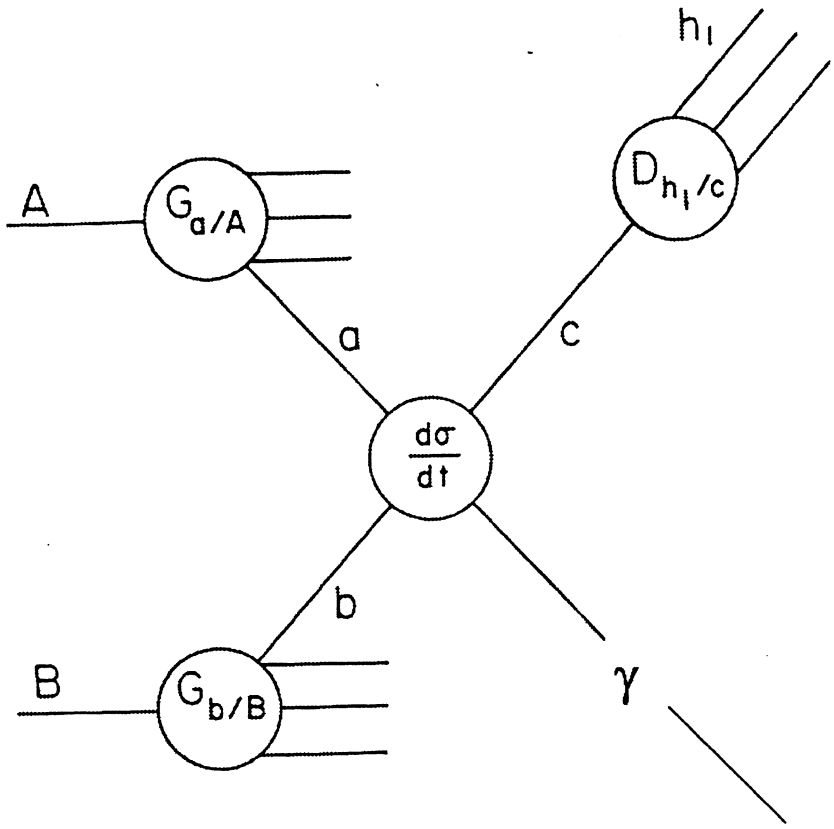

Figure 1.1: A Sketch of a $p\overline{p}$ Interaction. Proton 'A' and anti-proton 'B' each contribute a parton ('a' and 'b' respectively) to the perturbatively calculable parton scattering. The outgoing parton 'c' then turns into a jet.

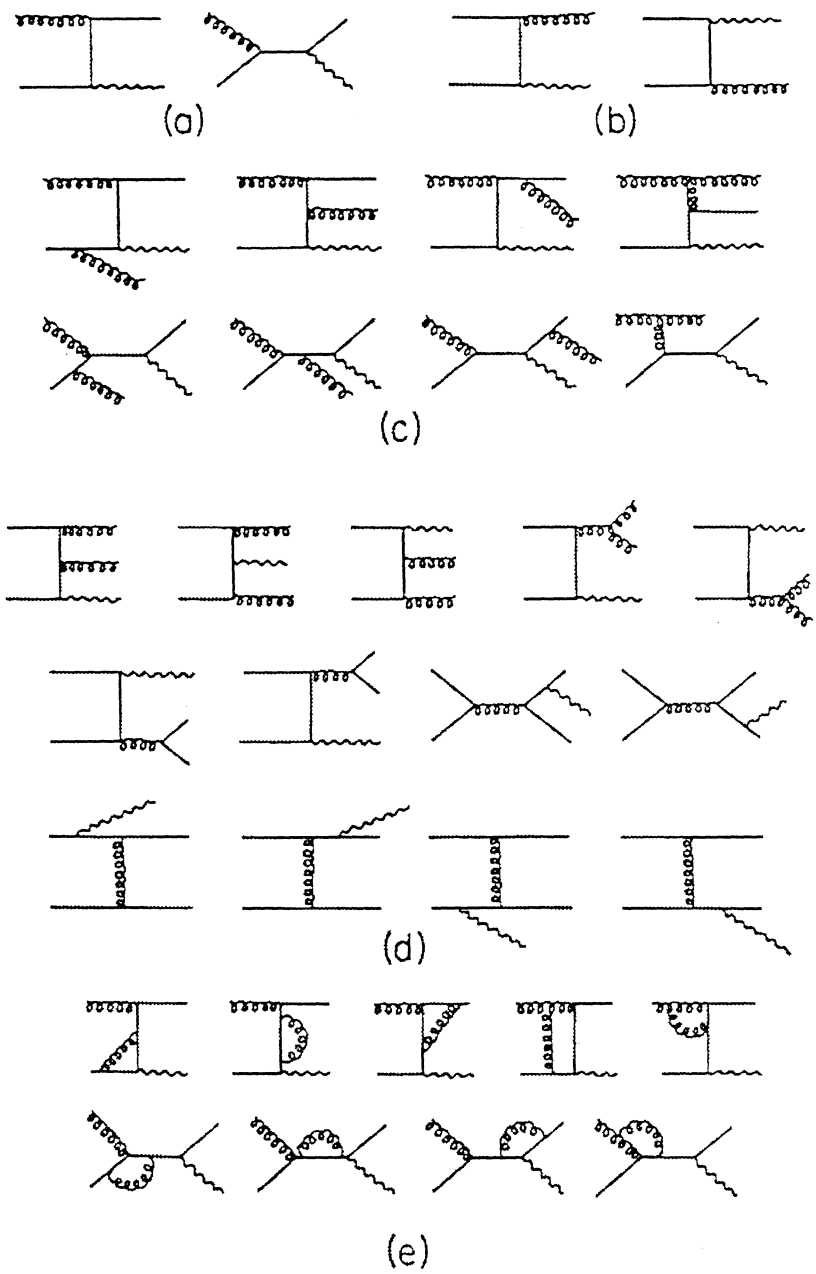

Figure 1.2: A Selection of Feynman Diagrams. The straight lines represent quarks and antiquarks, the helix spirals represent gluons and the wavy lines represent photons.

and gluons are obtained by a fit to all the data, with allowances for systematic experimental errors.

One important reason for measuring direct photon production cross sections in $p\bar{p}$ collisions is that they are sensitive to the gluon pdf. By contrast, the lepton on nucleon processes only directly probe the quark pdf, since quarks and leptons interact via the electroweak force whereas the gluons only interact via the strong force and hence are 'invisible' to the leptons. The measurement of the direct photon plus one and two jet(s) cross sections are made to test the descriptiveness of the perturbatively calculable QCD predictions to which the data are compared, because the perturbative part of the cross section explicitly predict the kinematics of the one or two outgoing partons (which turn into jets) in addition to that of the photon.

Although photons are produced copiously in $p\bar{p}$ collisions, most of them result from the decay of neutral mesons, particularly the π^0 and η. The largest source of background in the measurement of direct photons originates from jets which consist of a highly energetic neutral meson, accompanied by various other low energy particles. These neutral mesons decay quickly $\sim 10^{-13}$s into two photons which are very nearly colinear when the mesons have more than a few GeV/c of momentum. Two main methods to account for this background have been employed in previous measurements, direct background subtraction, and statistical background subtraction. In the direct method, the two photons from neutral meson decay are reconstructed independently on an event by event basis. This method requires a detector that is finely segmented spatially to resolve the two photons independently. The second method accounts for the background statistically, meaning that for a given set of data, the relative contributions of signal and background are determined, and the purity of the data sample is then included explicitly in the cross section calculation. A variation of the statistical background subtraction method is used in this analysis.

1.2 Some Previous Direct Photon Measurements

The first measurements of the direct photon cross section were made in the late 1970s by experiments at the CERN Intersecting Storage Rings at center of mass energies ($19 < \sqrt{s} < 63$ GeV). The Intersecting Storage Rings collided two beams of protons at an intersection angle of $\simeq 14°$ so the collisions occurred in a relativistically boosted frame of reference with respect to the laboratory. The first experiment (R806) [2] to design a detector to make precision measurements of direct photon production used two Lead / liquid Argon calorimeters placed one above the other about 2 meters from the interaction region, on the side away from the center of mass boost, in conjunction with a barrel scintillating detector circling the interaction region. This resolved the azimuthal angle of any charged particles that traversed it. The calorimeters were segmented finely enough to resolve single direct photons and each of the two photons which resulted from $\pi^0 \rightarrow \gamma\gamma$ decays, so the background was accounted for directly. One of the results of this early measurement was the observation of higher charged track multiplicity associated with π^0 production when compared to direct photon production. This enhancement was further studied by the R108 [3] experiment. This experiment had calorimeters on both the inside and outside of the Intersecting Storage Rings, as well as a more sophisticated charged particle tracking system. They used this system to determine the fraction of their data sample which was due to neutral meson background, based on the different probabilities for direct photons and multi-photon background to convert in the tracking chamber. Their results showed that direct photons were rarely accompanied by other particles, while π^0's and other neutral mesons were very often accompanied by other hadrons, meaning they were part of a jet. This was the first measurement of the photon plus one jet cross section, and the data was consistent with NLO predictions for $5 < E_T^\gamma < 10.5$ GeV [4]. Improvements in accelerator technology during the early 1980s led to the $Sp\bar{p}S$ collider, which explored the regions $\sqrt{s} = 540$, 630

GeV with the UA1 and UA2 detectors in collider operations, and $\sqrt{s} = 24.3$ GeV in a fixed target configuration at the UA6 collaboration [5, 6, 7]. Unlike earlier experiments, Both UA1 and UA2 collaborations used large general purpose detectors that covered the interaction region azimuthally, and out to within $\pm 5°$ of the beampipe in the polar angle. These detectors also were designed to measure both electromagnetic and hadronic energy, making jet measurements possible. The UA1 collaboration measured the inclusive isolated direct photon cross section and the isolated diphoton cross section. For both measurements, they relied on a statistical background subtraction procedure that used distributions of discriminant variables, formed for simulated signal and background events, as basis functions which were fit to the discriminant variable distributions of the data sample. The result of these fits was the purity, or fraction of the data sample due to direct photons. Both measured cross sections were well described by QCD calculations [5]. They also measured the polar angular distribution of photon plus jet events, and found it to be consistent with QCD predictions. The UA2 collaboration also measured the inclusive isolated direct photon cross section, and polar angular distributions of photon plus jet events and likewise found them to be consistent with QCD predictions [6]. In addition they used their data to extract the gluon structure function [8]. This function, which had to be obtained by fitting data, gives the probability that a gluon will have a particular fraction of the proton's (anti-proton's) momentum when it participates in a high momentum transfer (hard scattering) process. The UA2 method of background subtraction was also statistical in nature. It consisted of two steps. First, a set of cuts were imposed on each photon candidate in order to eliminate multiparticle QCD background. Then the purity was determined for the remaining sample by comparing the fraction of data events which converted to the fractions of simulated background and signal events which converted. The purity of the data sample was then calculated based on how close the data were to the simulated signal fraction,

relative to the difference between the simulated signal and background fractions. The UA6 collaboration operated a hydrogen gas target experiment at the $Sp\overline{p}S$ collider [7]. The detector was composed of tracking detectors placed before and after magnets, and electromagnetic calorimeters. It had two mirror image halves, placed immediately above and below the collider beampipe downstream with respect to the proton (or antiproton) beam. Background rejection was done in two steps. First, electromagnetic clusters that either had tracks pointing to them, or could be combined with another cluster to form an object with the mass of a neutral meson were rejected. The remainder of the background from events where the two showers could not be independently resolved or one of the photons from a neutral meson decay was not energetic enough to be reconstructed, was estimated using Monte Carlo techniques. The inclusive direct photon cross section for both $\overline{p}p$ and pp collisions was compared to theory, and as predicted the $\overline{p}p$ collisions had a higher cross section due to the contribution of the annihilation process ($q\bar{q} \rightarrow \gamma g$) [7, 9].

At Fermilab, the E706 collaboration studied direct photon production from processes with π^- and proton beams of momentum 500 GeV/c incident on Beryllium and Copper targets [10]. The detector's main elements were a large analysis magnet, a set of tracking chambers and a Lead / liquid Argon calorimeter that could measure both electromagnetic and hadronic energy deposition with high spacial resolution. The background was accounted for by a method similar to that of the UA6 experiment. The Collider Detector at Fermilab (CDF) made the first measurement of the isolated direct photon cross section at $\sqrt{s} = 1.8$ TeV in 1992 [11]. Their method of background subtraction was similar to that of the UA2 experiment. Improvements to the precision of this measurement were made in later years [12, 13]. In all cases, qualitative agreement was found, except for photons of low E_T [2] where

[2]Transverse energy is defined for any final state photon or jet as $E_T = E \sin\theta$ where θ is the usual polar angle.

the cross section was in excess of theoretical predictions. CDF has also measured the polar angle distribution of central isolated photon plus jet(s) events and found them to be in qualitative agreement with QCD predictions[14]. Unlike the UA1 and UA2 measurements, this was an inclusive measurement because it vectorially summed all the jets in the hemisphere opposite the photon into one 'summed' jet before the kinematics of the interaction were calculated. The first measurement of direct photon plus two jets cross cross section properties was made at CDF [15]. The cross section that they measured was larger than LO QCD predictions by a factor of two (which corresponded to 1.24σ for that measurement). However, the CDF's measurement of the direct photon plus two jets cross section was made with very little data, $\simeq 3.6\,pb^{-1}$ and the result quoted was the total photon plus two jet cross section, integrated over the kinematic region[3] that was used [15]. The measurement presented in this dissertation was made with $\sim 87\ pb^{-1}$ of luminosity, and is measured as a function of E_T^γ.

The DØ experiment has published a measurement of the inclusive isolated direct photon cross section in the central and forward polar regions [16]. The data are in good agreement with QCD predictions, except at low E_T, where the data are in excess of the theory. Other DØ studies of direct photon production include the polar angular distribution [17] of central isolated direct photons, which was in agreement with QCD predictions, and a search for quark compositeness [18] which established a lower mass limit for excited quarks at 531 GeV/c^2 at the 95% confidence level, using the theoretical model provided by U. Baur *et al.* [19]. Both of the latter analyses used jets, but were inclusive in that any number of jets in any detectable kinematic or fiducial region were allowed. The measurement presented here places

[3]The kinematic region included events that satisfied: $25 < E_T^\gamma < 54$ GeV, $|\eta^\gamma| < 0.9$, $E_T^{jets} > 20$ GeV, $|\eta^{jets}| < 2.0$, and all objects separated by $\Delta R = \sqrt{(\delta\phi)^2 + (\delta\eta)^2} > 0.8$. The variable η is pseudorapidity, defined as $\eta \equiv -\ln\tan\frac{\theta}{2}$.

explicit constraints on the number of jets and their kinematics, allowing for a more accurate comparison to QCD predictions. All DØ photon analyses use a statistical background subtraction method which is similar to the UA1 method, and is outlined in Chapter 3.

1.3 The Dissertation

This dissertation will describe all essential elements of the analysis. The detector components used in the analysis will be reviewed, including offline processing. The photon plus one and two jet cross sections will be introduced, along with the details of the offline analysis including: fiducial cuts, event selection cuts, kinematic cuts, photon candidate selection cuts, the efficiencies of all the cuts, and the data sample background calculation. The Monte Carlo techniques that generated the events used in determining the background of the data sample will then be explained. Next, the theoretical calculations that the data are compared to will be discussed. Finally the errors on the measurement will be discussed, and the conclusions of the analysis given. The photon plus one jet cross section is in good agreement with the NLO theory in all kinematic regions. The photon plus two jets cross section is in agreement with the theory when events with low E_T jets ($E_T < 55$ GeV) are predominant. Low statistics limit the reliability of the cross section measurement of events with jets of larger E_T.

CHAPTER 2
THE DØ DETECTOR

The DØ detector was designed to measure the momentum of high energy electrons, muons, photons and jets produced in $p\bar{p}$ collisions at the Tevatron. DØ is comprised of sub-detectors, functionally categorized into tracking, calorimetry, and muon detection. Figure 2.1 shows the calorimeter and tracking components.

A right handed coordinate system is defined in the detector where the z axis is the direction of the protons as they pass through the detector and the y axis points up. DØ analyses use pseudorapidity $\eta = -ln(tan(\frac{\theta}{2}))$, where θ is the polar angle. This analysis uses only events that have a central photon, where $|\eta^{\gamma}| < 0.9$.

Tracking components are the vertex (VTX), central and forward drift chambers (CDC and FDC), and transition radiation detector (TRD). Surrounding these is the calorimeter which measures the energies of electrons, photons, and jets. It will be sufficient to briefly describe the CDC and calorimeter, focusing on their capacities in the measurement of final states involving a photon and one or more jets. A complete description of the detector is given in reference [20].

2.1 Tracking in DØ

The CDC is a set of four concentric tracking chambers, each with 32 azimuthal cells. It covers the central region out to $|\eta| = 1.1$ Each cell measured the quantity and location of ionization produced by the charged particles that traversed it using seven sense wires and two delay lines for $r - \phi$ and z charge localization respectively. A fit to the signals of the CDC allowed the determination of a charged particle's

trajectory to within $300\mu m$ in $r - \phi$ and $\sim$ 2 mm in z. The efficiency of track reconstruction was dependant on the number of neighboring tracks, and thus on the number of jets in an event. It was measured using $Z \rightarrow e^+e^-$ + jet(s) events as 86.9% $\pm$ 9.9% and 75.8% $\pm$ 28.2% for electrons plus one and two jet(s) events respectively. The definition of tracking efficiency is the probability of reconstructing the track of a real electron. The study that produced the above efficiencies used a tag and test method [21]. Used with a sample of events that had two electromagnetic calorimeter clusters and one or two jets, this method required one of the two electromagnetic calorimeter clusters to pass a set of 'tag' cuts designed to select only electrons produced by Z decays. The 'test' cluster was then checked for a reconstructed track that pointed to it. The efficiency of track reconstruction was then the ratio of events which had a 'test' cluster with a track pointed within $R = \sqrt{(\Delta\eta)^2 + (\Delta\phi)^2} = 0.2$ of it's centroid to the number of events with a 'tag' electron for the one and two jet cases respectively.

Reconstructed tracks were used in this analysis to reject electromagnetic calorimeter clusters that were produced by electrons, converted direct photons, and charged hadrons. Approximately 9% of all photons converted in the VTX and TRD before reaching the CDC. These events were rejected since background from [π^0 or η] $\rightarrow \gamma\gamma$ decays were twice as likely to convert and produce charged tracks. The probability for a direct photon to convert is given by

$$P(x) = 1 - e^{-\frac{7x}{9X_0}}$$

where $\frac{9X_0}{7}$ is the conversion length and x is the distance the photon has traveled through the relevant media. The radiation length (X_0) characterizes the radiative energy loss of an electron in a particular medium. It is defined as the depth that the average electron has penetrated to when it's initial energy has been reduced by a factor of e.

Corrections were applied to the cross sections to account for events lost due to conversions and track overlap (which occurred when a charged track from an underlying event intersected with a direct photon's calorimeter cluster). The probability for track overlap in the CDC was measured as $.10 \pm .02$ [22]. See section 3.7.1 for details.

2.2 Calorimetry in DØ

The detector used a liquid Argon / Uranium sampling calorimeter to measure particle energies. The calorimeter was contained in three cryostats that surrounded the tracking detectors. The central calorimeter covered the rapidity range $|\eta| < 1.2$, and the two forward calorimeters each covered the range $0.7 < |\eta| < 4.5$. The overlap was due to the detector's cylindrical geometry.

The calorimeter is functionally partitioned into electromagnetic (EM) and hadronic (HAD) calorimeters. The central electromagnetic and hadronic calorimeters were made of 32 and 16 identical azimuthal modules respectively. The electromagnetic calorimeter had four layers, each of which could be read out independently. In units of radiation length X_0 the layers were approximately 2, 2, 7, and 10 X_0 thick respectively. The hadronic calorimeter's thickness, measured in nuclear interaction lengths Λ, varied as a function of pseudorapidity but was $\sim 7\ \Lambda$ over the entire pseudorapidity range. The interaction length is the mean free path of a hadron in matter, so the probability of a hadron penetrating to a depth x without interacting is

$$P(x) = e^{-\frac{x}{\Lambda}}$$

Both the electromagnetic and hadronic calorimeters are partitioned into assemblies of readout cells arranged so that the cell centers lie along lines of fixed η and ϕ at intervals of .1 in each. These cell collections are referred to as calorimeter *towers*, each of which pointed to the geometric center of the detector. They were pseudo-projective because the edges of every tower's cell did protrude into neighboring towers. For better spatial resolution of electromagnetic showers, the segmentation was increased to $.05 \times .05$ in the third electromagnetic calorimeter layer (EM3). The transverse energy of a final state photon or jet is defined as $E_T = E \sin\theta$, where E is the energy and θ is the polar angle of the centroid of energy deposition. The missing E_T in an event was the additive inverse of the vector sum, in the x - y plane, of the E_T of all calorimeter cells, and was corrected for muon E_T, which was only partially measured by the calorimeter. The calorimeter's energy resolution has been measured for electrons and pions as $\delta E \simeq .15\sqrt{E(GeV)}$ and $\delta E \simeq .50\sqrt{E(GeV)}$ respectively. The electromagnetic calorimeter had linear response to energy deposition to within 0.2% [23]. The calorimeter's electromagnetic to hadronic response ratio was measured ~ 1.1, and jet energy corrections were applied during reconstruction to account for this non-equality [24].

To test the calorimeter's response to energy deposition in detail, several central calorimeter modules were constructed and operated in a *test beam* configuration. The modules were placed in front of beams of electrons and hadrons with energies between 7.5 and 100 GeV, and their response was measured. The results of the test beam runs were used in part to study the detector's energy response and to configure efficient online triggers.

2.3 Triggering in DØ

The trigger system had three levels (0-2), each of which passed events of interest. Level 0 (L0) and level 1 (L1) were implemented in hardware because they needed to handle data at rates of $\sim$ 300k and $\sim$ 1kHz respectively. Level 2 (L2) was implemented on a farm of VAX 4000/60 computers. Level 2 handled an input rate of $\sim$ 100 events per second and wrote 2-4 events per second to tape for offline reconstruction.

2.3.1 Level 0

Level 0 consisted of scintillating tiles connected to photomultiplier tubes which were all mounted on the inside faces of the forward cryostats. The pseudorapidity coverage of the tiles was complete between $2.2 < |\eta| < 3.9$ and partial between $1.9 < |\eta| < 4.3$. The signals from L0 were used to determine the z vertex of an event, and to measure luminosity.

The z axis location of an event could be located to within 4 cm, if only one interaction occurred, by measuring the time differential between the signals of the forward and backward counters. The resolution of this measurement was degraded if more than one hard scattering occurred because of the ambiguity introduced by multiple signals on each side.

L0 counted scintillator hits during each bunch crossing, and added them to the run total. The technique for making the luminosity measurement depended on the world average measurement of the total inelastic $p\overline{p}$ cross section and Monte Carlo simulation of the L0 scintillator response to inelastic scattering. Previous experiments [25, 26, 27, 28] have measured the total inelastic cross section for $p\overline{p}$ collisions as $\sigma_{in} = 58.9$mb at $\sqrt{s} = 1.8$ TeV. The L0 efficiency for detecting inelastic processes (ϵ_{L0}) was estimated using a simulation. This yielded a minimum bias (MB) cross section for DØ ($\sigma_{MB} = \epsilon_{L0}\,\sigma_{in} = 48.2$mb). Measuring energy deposition in the scintillators then yielded a measurement of the observed luminosity, from which the actual, unbiased luminosity was obtained. The 6% error associated with

the luminosity was mainly due to uncertainty in the world average total inelastic $p\bar{p}$ cross section measurement.

2.3.2 Level 1

Level 1 summed the electromagnetic (EM) and hadronic (HAD) energy in sets of calorimeter towers of dimension $.2 \times .2$ in $\eta \times \phi$ space. Each of these summed sets of calorimeter towers, called trigger towers, was then compared to a reference list of 4 E_T thresholds for EM only, HAD only, and EM+HAD. A typical direct photon L1 requirement was at least one trigger tower with more than 25 GeV of EM energy deposited in it. L1 could also be set to prescale any of the 32 L1 triggers. Prescaling sent to L2 a fraction of events that passed the L1 trigger requirements, reducing the usage of the slower L2 trigger. The L1 prescaling factor for direct photons was varied between 1 and 5 for instantaneous luminosities between $4-20 \times 10^{30} / (s\, cm^2)$.

2.3.3 Level 2

Level 1 passed the list of trigger towers that satisfied the trigger list terms to the Level 2 processors that ran a fast clustering and isolation routine which formed energy clusters and applied a set of cuts on the cluster designed to reject background events. For each electromagnetic trigger tower that L1 passed to L2, the following clustering algorithm was used. The cluster center was defined as the center of the calorimeter tower (in the L1 trigger tower) that had the most energetic cell in EM3. The cluster energy was then the sum of the energy in the electromagnetic calorimeter and the first layer of the hadronic calorimeter in a region $\Delta\eta \times \Delta\phi = .3 \times .3$ centered about the central cluster tower. Then the cluster was discarded if: its E_T was not above the L2 threshold, more than 10% of the cluster energy was hadronic, the cluster's fractional energy deposition in EM3 was not in the range (10%<EM3<90%), an η dependant shower shape cut was failed, or the energy in the

isolation region was greater than 15% [1] of the cluster energy, ($\frac{E_T^{R=0.4} - E_T^{Cluster}}{E_T^{Cluster}} < .15$). The shower shape cut was the difference in the second moment of energy deposition in the cluster and a $.5 \times .5$ area centered on the cluster. These cuts were tuned to be fully efficient for test beam electrons [29].

After an event passed level 2, the detector's raw data was written out to magnetic tape for offline processing, unless the level 2 prescale for that trigger rejected it. Prescale factors were varied between 1 and 200 depending on the average instantaneous luminosity and the trigger's E_T threshold.

It was necessary to obtain small samples of detector data which were not biased by triggering conditions. For this purpose, minimum bias and zero bias events were taken. A zero bias event only required that a proton-antiproton bunch crossing occur. A minimum bias event only required that both sides of the L0 scintillators measured energy deposition.

2.4 Event Reconstruction

The offline reconstruction program used the digitized signals from all detector components, and performed a complete reconstruction of each event. It correlated energy deposition in the calorimeter with fits to the tracking chambers's signals, allowing particle identification. The global detector fits, to tracking and calorimetry data combined, also reduced ambiguities in track reconstruction due to charged track multiplicity in the tracking chambers.

The offline reconstruction also made use of refinements to detector calibration, which evolved over the course of the run. Furthermore, most of the data was reconstructed several times as reconstruction algorithms were fine-tuned with data.

[1] 30% for the lowest E_T trigger.

For example, since the absolute energy scale of the calorimeter was determined from reconstructed $Z \rightarrow e^+e^-$ events, the precision of the measured mass increased with higher statistics. Once the electromagnetic energy scale was determined from the reconstruction of Z's, it was necessary to establish the hadronic calorimeter's energy scale. From measurements at the DØ test beam, it was known that the calorimeter's response was $\simeq 10\%$ lower for charged pions than for electrons with a momentum greater than 10 GeV/c. Since most DØ analyses use jets, it was necessary to obtain the calorimeter's jet energy scale.

The jets observed in collider operation vary widely in particle multiplicity and individual particle energy, due to fragmentation and hadronization effects. They also contained a large number of very low energy particles to which the calorimeter had a non-linear response. The DØ approach to this calibration problem was to use real jets with corrections derived from Monte Carlo simulations of single particle showers. The corrections to hadronic jet energy were given by

$$E_{jet} = \frac{E_{meas} - O}{(1 - S)R_{had}}$$

where O was the offset due to Uranium noise, event pileup (energy remaining in the calorimeter from a previous bunch crossing), and the underlying event. These contributions to O were measured together using minimum bias events. The quantity S corrected for jet particles that were at the edge of the jet cone, and so deposited some of their energy outside the cone. This factor was determined by Monte Carlo simulation and test beam data. Finally, R_{had} was the correction made to compensate for the calorimeter's reduced response to hadronic energy deposition compared to electromagnetic energy.

$$R_{had} = 1 + \frac{\vec{\not{E}_T} \cdot \hat{n}_\gamma}{E_T^\gamma}$$

It was measured using both dijet events, where one of the jets fragmented in an isolated EM cluster, and photon plus jet events. The necessary correction was

computed by balancing the $\not{E}_T$ along the direction of the electromagnetic cluster. Projecting the $\not{E}_T$ onto this axis minimized the effects of any inherent transverse momentum the entire two body final state might have. The jet energy correction was on the order of 10-15% throughout the E_T^{jet} and η^{jet} ranges used in this analysis.

The photon clustering algorithm used the sum of the energy in each $.1 \times .1$ electromagnetic calorimeter tower, plus the energy deposited in the first layer of the hadronic calorimeter. A list of all such towers with more than 1.5 GeV was formed, then all neighboring towers with more than 50 MeV were added together, forming a cluster. Clusters that were not at least 90% electromagnetic or had more than 40% of their energy outside the most energetic tower were discarded. From test beam measurements, these cuts were determined to be > 99% efficient for real electrons. The cluster centroid was determined by a *log*E weighted vector sum of the member towers (EM calorimeter + first HAD layer). Finally, several variables were computed which further characterized the clusters. The shower shape was compared to the test beam measurement of the electron shower shape using a χ^2-like variable. The test [30, 31] was formed by defining a covariant matrix of electron shower observables x_i using N electrons

$$M_{ij} = \frac{1}{N}\sum_{n=1}^{N}(x_i^n - \bar{x}_i)(x_j^n - \bar{x}_j)$$

where x_i^n is the value of observable i for electron n and $\bar{x}_i$ is the mean value of observable i for the sample. Then the quantity

$$\chi^2 = \sum_{i,j}(x_i^k - \bar{x}_i)M_{i,j}^{-1}(x_j^k - \bar{x}_j)$$

could be formed for cluster k. Forty-one observables were used, and M_{ij} was constructed for every electromagnetic calorimeter tower in η. The observables included were: fractional energy deposition in EM layers 1,2, and 4, fractional energy in each cell in a 6×6 cell window in the third layer of the electromagnetic calorimeter (EM3) , the logarithm of the cluster energy $log_{10}E$, and a characterization of the

z vertex position ($\frac{z}{\sigma_z}$). Also the electromagnetic and hadronic E_T were formed in cones of radius $R = \sqrt{(\Delta\eta)^2 + (\Delta\phi)^2} = 0.2$ and 0.4, allowing for the calculation of the photon isolation E_T^{iso}.

The jet finding algorithm similarly formed an energy ordered list of calorimeter towers (EM + HAD) with more than 1 GeV. For each tower on the list, the energy of all towers within a radius $R = \sqrt{(\Delta\eta)^2 + (\Delta\phi)^2} < 0.3$ were added together. The E_T weighted centroid of this object was used as the center of a $R = 0.7$ jet cone. The E_T weighted center of this new object was then calculated, and the process repeated until the jet centroid stabilized. In the event that two jets overlapped, they were split if the shared energy was less than 50% of either jet's energy, otherwise they were combined.

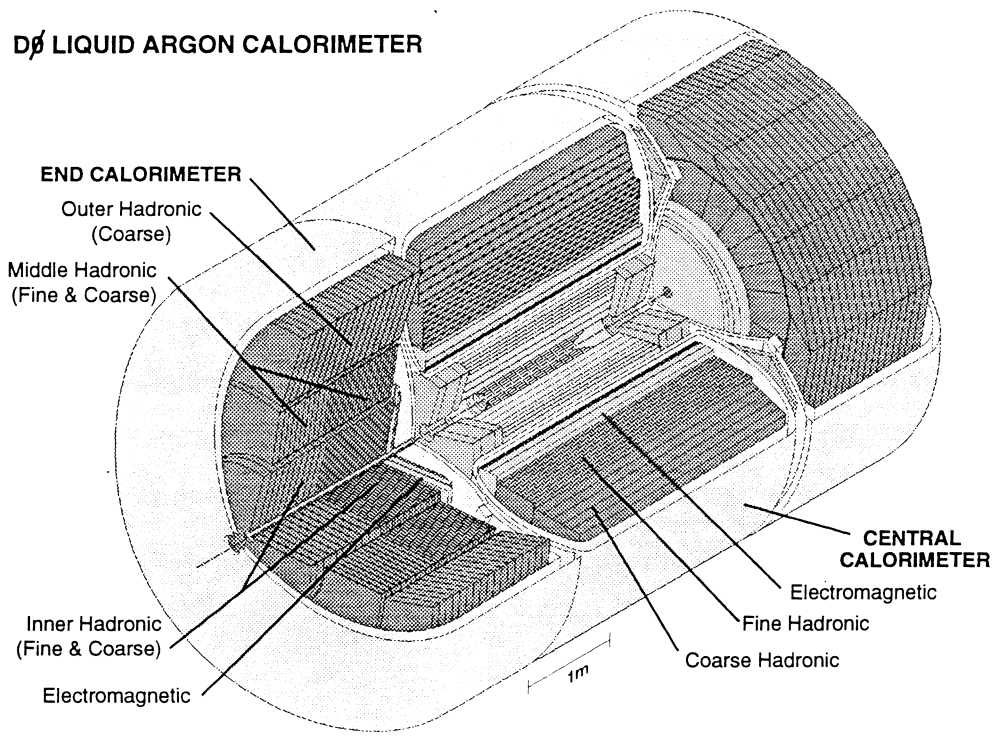

Figure 2.1: The DØ Calorimeter and Tracking Chambers. This view emphasizes the calorimeter's segmentation into three cryostats, and electromagnetic and hadronic modules. The tracking chambers are inside the central calorimeter cryostat.

CHAPTER 3

THE ISOLATED PHOTON + JET(S) CROSS SECTIONS

3.1 The Cross Sections $\sigma_{\gamma+Jet}$ and $\sigma_{\gamma+2Jets}$

The cross sections of the photon + jet and photon + 2 jet final states, $\sigma_{\gamma+Jet}$ and $\sigma_{\gamma+2Jets}$ respectively, were given by

$$\frac{d\sigma}{dE_T^{\gamma}d\eta} = \frac{NP}{\mathcal{L}\Delta\eta\Delta E_T A\epsilon_s\epsilon_m\epsilon_t\epsilon_j\epsilon_o}$$

where N was the number of candidate events, P was the purity of photon candidates, $\Delta\eta$ was the rapidity coverage, ΔE_T the bin size, A was the geometric acceptance of fiducial cuts, ϵ_s was the efficiency of photon candidate selection cuts, ϵ_m was the efficiency of the $\not{E}_T$ cut, ϵ_t the efficiency of the charged track rejection cut, ϵ_j was the efficiency of jet reconstruction and jet quality cuts, and ϵ_o was the efficiency of the single photon trigger used online. was simpler due to all the cancellations.

3.2 Data Sample

The data sample for this analysis was taken during the 1994-1996 1b Tevatron collider run. Several different triggers were used to take the data. The three low E_T threshold triggers were prescaled to allow data taking at different luminosities. The data were partitioned into regions such that one and only one fully efficient trigger ($\epsilon_o = 1.0$) populated it. The four triggers used are summarized in table 3.1

Because some photons showered on the boundary between two or more trigger towers, splitting its energy between them, the trigger system did not operate at full

efficiency for photons of an E_T just above the trigger threshold. The trigger efficiency was estimated as a function of E_T^γ using Monte Carlo photons. Direct photon events [1] were generated, the calorimeter's response simulated, and the trigger system behavior emulated. The efficiency was then computed relative to all the offline cuts as a function of E_T^γ. Figure B.1 in Appendix B shows the trigger efficiencies as a function of E_T^γ. The results of this study indicated that each trigger was highly efficient ($\sim$ 99%) in the ΔE_T^γ analysis bin(s) that it was used to populate.

Table 3.1: Initial Data Sample. Columns show the triggers used, level 2 trigger threshold, the luminosity recorded for each trigger, the E_T^γ range for which it was used, the number of events taken by that trigger in the specified range. Each of the first three triggers was prescaled differently, yielding different effective trigger luminosities. All luminosities have a 6% systematic error associated with them.

Trigger	$E_{T_{L2}}^\gamma$ (GeV)	$\int \mathcal{L}dt(pb^{-1})$	E_T^γ (GeV)	N_{events}
GAM_6_ISO_GAM	6	0.0127	10 to 20	15,878
GAM_14_ISO_GAM	14	0.21	20 to 30	5,614
EM1_GIS	25	13.5	30 to 50	95,283
EM1_GIS_HIGH	45	87.	50 to 100	90,445

[1] For more information on simulated direct photons see Chapter 4

3.3 Fiducial Cuts

Fiducial cuts were placed on all events so that the photon and jet(s) were in well understood regions of the detector. Each event was required to have a central vertex, ($|Zvertex| < 50cm$). The efficiency of this cut was estimated for each trigger by applying all other fiducial and event selection cuts (see section 3.7). The efficiency was then the ratio $\epsilon_{Zvertex} = \frac{N_{Pass}}{N_{Total}}$ [2]. The cut ($|\eta^{\gamma}_{det}| < 0.9$) ensured that photons showered entirely within the central region of the calorimeter.

A cut was made to ensure that the photons were away (>2 cm) from the electromagnetic calorimeter module boundaries. Table 3.3 shows the efficiencies for each filter, and the resulting geometric acceptance factor (A) after folding in the efficiency of the ϕ_{γ} cut (0.80).

Trigger	E_T^{γ} (GeV)	$\epsilon_{Zvertex}$%	A %
GAM_6_ISO_GAM	10 to 20	94.09	75.27
GAM_14_ISO_GAM	20 to 30	94.09	75.27
EM1_GIS	30 to 50	93.06	74.45
EM1_GIS_HIGH	50 to 100	93.19	74.55

Table 3.2: Z Vertex Cut Efficiency from Data. The efficiencies quoted for the z vertex cut were accurate to within 10^{-4} since they were measured using each trigger sample in its entirety, however, binomial errors were assigned to them on a point by point basis in the analysis to account for statistical fluctuations.

[2]Binomial errors were assigned to this and all other data-estimated efficiencies on a point by point basis using the number of data points in the data bin as the sample size.

3.4 The Kinematic Region

Further cuts were applied to the jet(s) in each event to ensure that they were in a well understood region of the detector and had sufficient energy to be reconstructed 100% of the time [32]. These were $|\eta^{Jet}| < 2.5$ and $E_T^{jet} > 25$ GeV. Two angular separation cuts were applied, $\Delta R_{\gamma,jet(s)} > 0.7$ and $\Delta R_{jet_1,jet_2} > 0.7$. These cuts *defined* the kinematic regions used in this analysis, and as such had no cut efficiency associated with them.

3.5 Missing E_T Cut

A cut on the maximum allowable missing transverse energy in an event, $\not{E}_T < 20$ GeV, was made to ensure that the photon and jet(s) were well measured. It suppressed the small background from $W \rightarrow e+\nu+jet(s)$ events as well as events where a jet was not well measured due to a large jet showering fluctuation or calorimeter noise. The efficiency of this cut was estimated from the data using events that passed all other cuts in the analysis in the denominator of the expression $\epsilon_m = \frac{N_{pass}}{N_{total}}$. A sample plot of the efficiency of this cut is shown in figure 3.1.

3.6 Jet Cuts

The cuts imposed eliminated fake 'main ring' jets that were due to main ring energy deposition in the calorimeter and electronic noise. If a jet failed any of these cuts it was not considered so if the event passed all other cuts, it could still be counted in the appropriate cross section. A cut was placed on a jet's electromagnetic

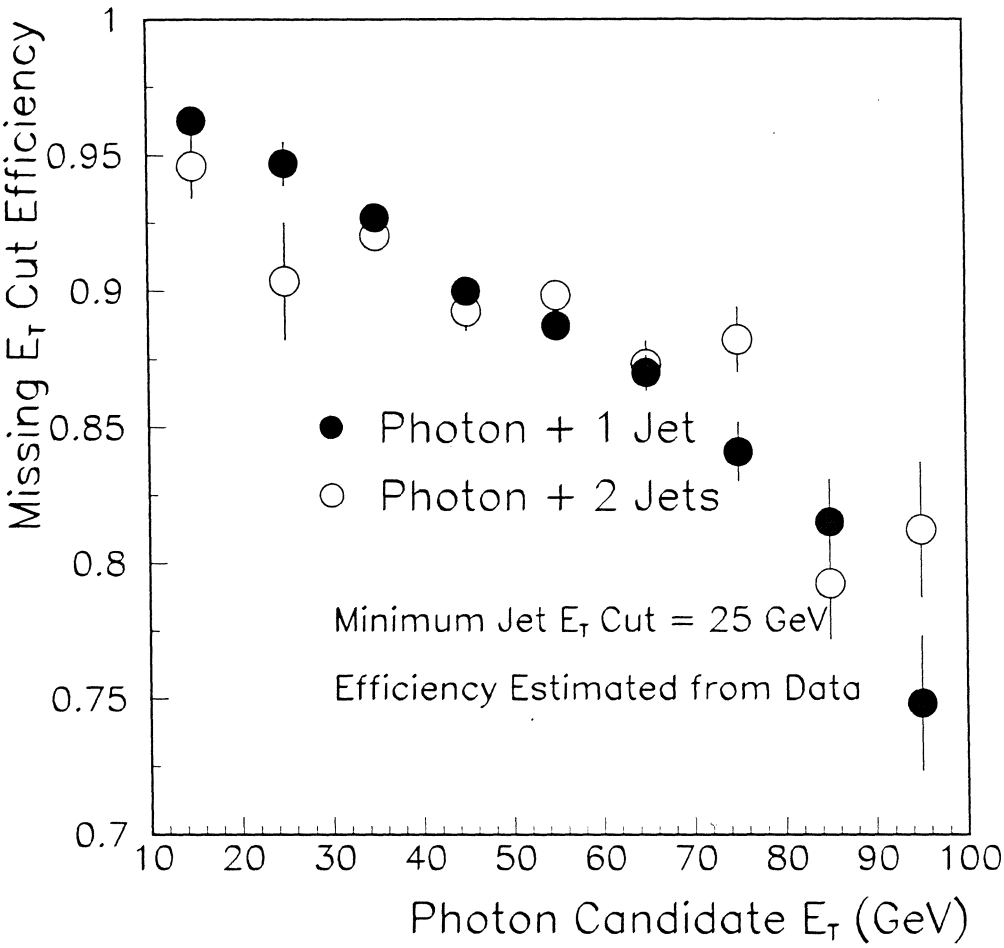

Figure 3.1: Data Based Estimate of the missing E_T cut efficiency ϵ_m, plotted with statistical errors.

energy fraction, $0.05 < \frac{E_{EM}}{E_{EM+HAD}} < 0.95$, to suppress fake jets from 'main ring' events, which occur when protons from the main ring accidentally collide with the uppermost part of the hadronic calorimeter, depositing energy that would otherwise be counted as part of a jet. It also eliminated the possibility of counting a photon as a jet.

The hot cell fraction was defined as the ratio of the energies in the most energetic cell to the next most energetic cell in a particular jet. The cut on this quantity, $Hot\ Cell\ Fraction < 10.0$, eliminated fake jets caused by noise in the calorimeter electronics.

The coarse hadronic fraction was the ratio of a jet's energy measured in the outermost layer of the calorimeter to the total jet energy. By imposing the cut $Coarse\ Hadronic\ Fraction < 0.4$, main ring jets that might have passed the electromagnetic fraction cut - due to energy deposited by a real jet - are excluded ~100 % of the time.

The total efficiency, after the application of the cuts above and the $E_T^{jet} > 25$ cut, was $\epsilon_j = (96.9 \pm .3)\%$. This factor was used for single jet events and its square was used for two jet events $\epsilon_{Jets} = (93.9 \pm .4)\%$ [33]. Figure 3.2 shows the distributions of the variables, and the cuts.

3.7 Photon Candidate Selection Cuts

Next a set of photon candidate selection cuts was made to restrict contamination of the data sample by multiparticle QCD background. The isolation cut, $E_T^{R=0.4} - E_T^{R=0.2} < 2\,GeV$, required that less than 2 GeV of E_T was in the annular region surrounding the electromagnetic energy cluster between .2 and .4 in $\eta \times \phi$ space. The electromagnetic fraction cut, $E_{em}/E_{total} > 0.96$, required that the candidate

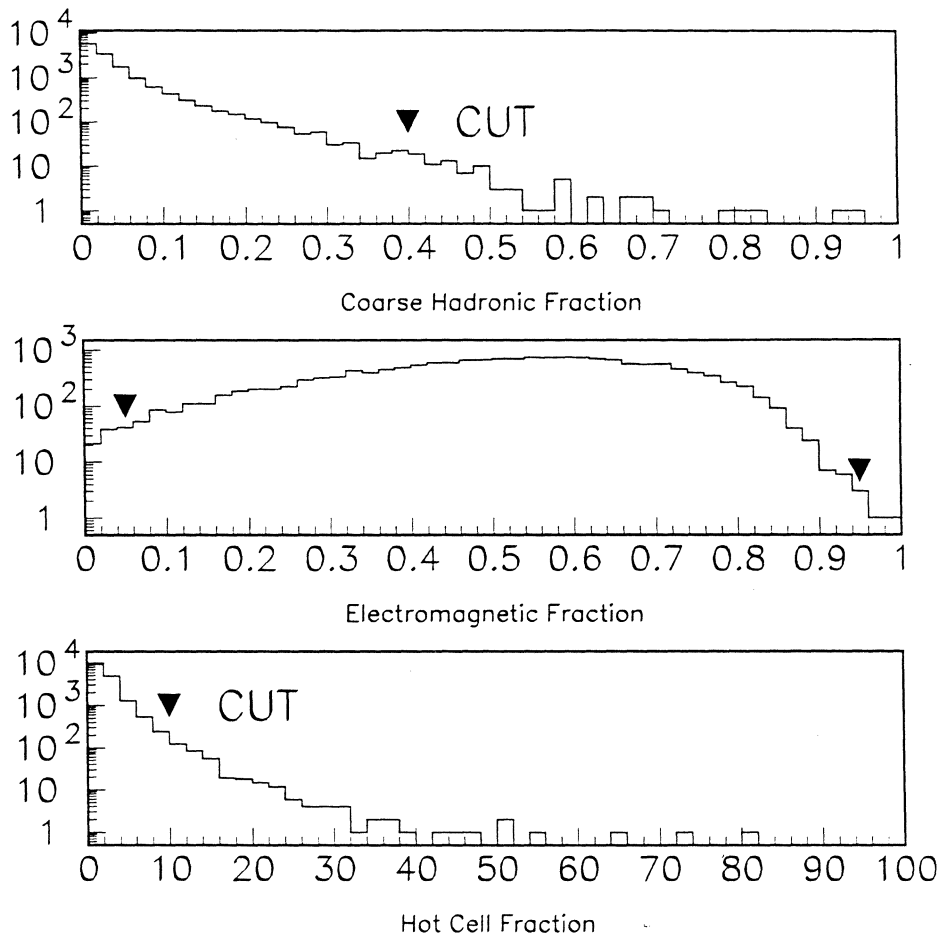

Figure 3.2: Standard Jet Cuts. The events from which these data were taken had: a photon candidate $E_T^\gamma > 30$ GeV that passed all selection cuts, one and only one jet $E_T^{jet} > 30$ GeV in the fiducial region $|\eta^{jet}| < 2.5$, where the photon and jet were well separated $R_{\gamma,jet} > 0.7$. The triangles show the placement of the three cuts. The electromagnetic fraction cut accepted jets between the two triangles.

deposited more than 96% of its energy in the electromagnetic calorimeter. To further reject hadrons, a cut was placed on the electromagnetic shower shape variable χ^2. To pass, a trigger photon must have had $\chi^2 < 150$.

The combined efficiency of these cuts was determined from simulated photons which had minimum bias event calorimeter energy added to them. Figure 3.3 shows the combined efficiencies of these selection cuts as a function of E_T^γ, while figure 3.4 shows the distributions of the variables and the cuts.

3.7.1 Charged Track Cut

An additional cut was placed on the photon candidate, the requirement that no charged track be found in the CDC within $R = \sqrt{(\Delta\eta)^2 + (\Delta\phi)^2} = 0.2$ of the cluster centroid. The efficiency of this cut was given by $\epsilon_t = 1 - Pt - W(1 - P^2)$ where P was the probability for a single central photon to convert to two electrons before reaching the CDC, t was the probability of reconstructing a track in the CDC from a charged particle, and W was the probability for a charged track from an underlying event to intersect with a direct photon [34]. This cut eliminated most real electrons, converted direct photons, and direct photons that had a track from an underlying event pointing at its calorimeter energy cluster. From references [22] and [21] the efficiencies of this cut were obtained. Table 3.3 gives the results.

Table 3.3: Charged Track Cut Efficiencies.

Quantity	
t	0.83 ± 0.01
W	0.10 ± 0.02
ϵ_t	0.82 ± 0.18
P	0.088 ± 0.009

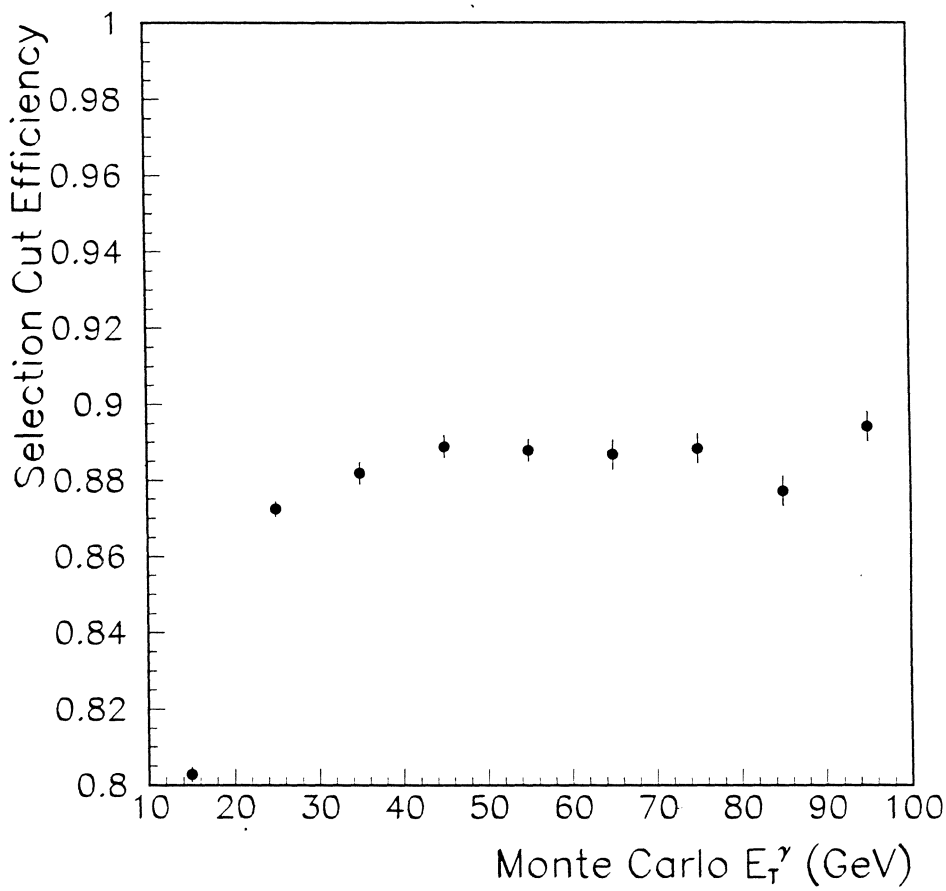

Figure 3.3: Photon Candidate Selection Cut Efficiency as Determined from MC Photons as a Function of E_T^γ.

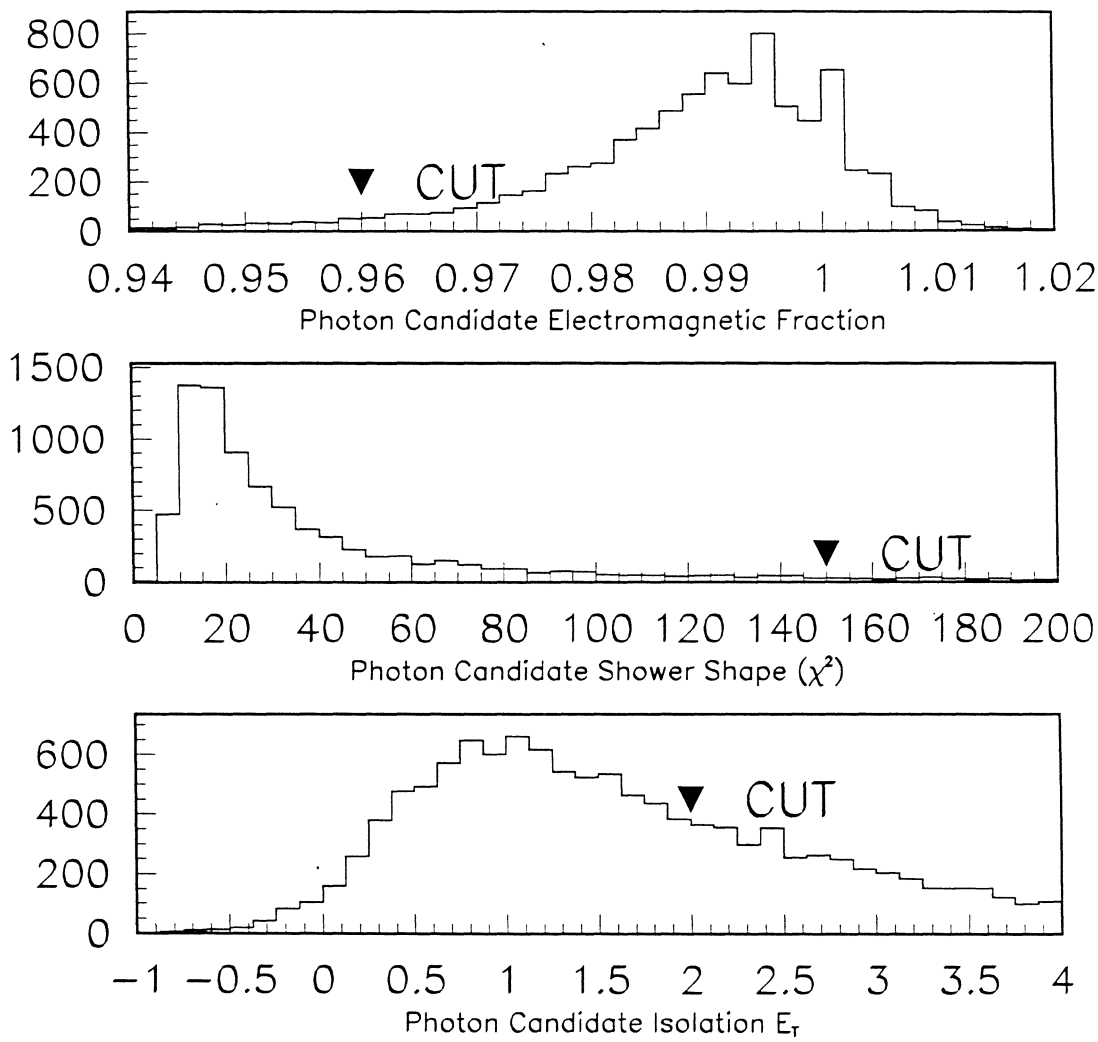

Figure 3.4: Photon Selection Cuts.

3.8 Photon Background Subtraction

The ratio of energy deposited in the first layer of the electromagnetic calorimeter to the total energy of the cluster was used to discriminate between photons and jets.

In order to determine the differences in how photons and jets deposited energy in the electromagnetic calorimeter, two sets of Monte Carlo (MC) events were produced with the Pythia [35] event generator: one of photons, and one of jets that gave most of their energy to a π^0 or an η. All these events were run through the detector simulator program, had zero bias calorimeter energy added and then were reconstructed. The resulting sets of data then had realistic MC signal (γ's) and background ($jet \rightarrow [\pi^0 \text{ or } \eta] \rightarrow \gamma\gamma$) events respectively. As expected, the reconstruction program found photon-like objects in both MC samples. Photon candidate selection cuts were applied to both datasets. The discriminant variable, $log(EM1/EM_{total})$, used the ratio of the energies a cluster deposited in the first layer of the electromagnetic calorimeter to the total cluster energy. The logarithm emphasized clusters that deposited very little of their energy in the first layer. Figure 3.5 shows normalized distributions of the discriminant for data, MC photon candidates and MC jets. Note that in the region where the discriminant variable was less than -2, both the data and MC photons had tails which were large compare to the MC jets. The jets were overwhelmingly multi-photon clusters, which meant that they were much more likely to undergo conversion in the first layer of the electromagnetic calorimeter, depositing energy there, which in turn increased the discriminant variable. The photon purity was extracted by using the two MC distributions as basis functions for a one parameter fit to the photon candidates [5]. The weighted sum of the two MC distributions was fit to the data using a maximum log likelihood procedure. The weighed sum took the form $F(P,x) = PD_{Photons}(x) + (1-P)D_{Jets}(x)$, where the fit parameter was constrained ($0.0 < P < 1.0$), $D(x)$ were the MC distributions of the discriminant variable, and F was fit to the photon candidates. The fit of the

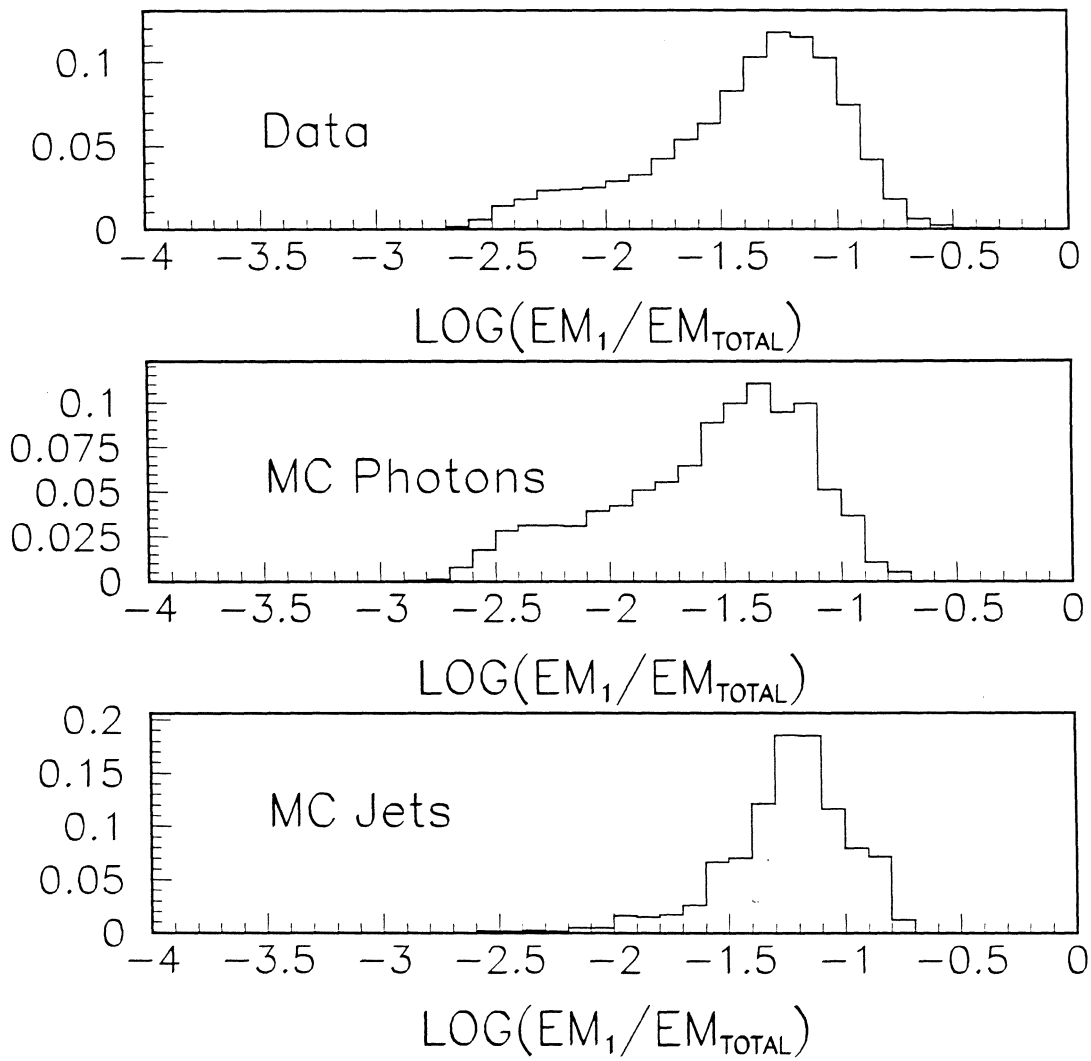

Figure 3.5: Discriminant Variable of Data, MC Photons and MC Jets. The area under each curve was normalized to unity to emphasize the shape difference. For all three plots $30 < E_T(GeV) < 40$.

data shown in figure 3.5 is shown in figure 3.6. Figure 3.7 shows measured photon purities for the 1 and 2 jet cases as a function of E_T^γ. A log scale was chosen for the plot to emphasize the fact that the calorimeter's response is well modeled to better than 1% over two decades of dynamic range. The small right hand tail of the distribution is due to a small fraction of photon candidates that showered across calorimeter towers, and had the interaction vertex position mis-measured. During event reconstruction, the convolution of these two effects resulted in poorly measured clusters, producing the tail in the data distribution. The Monte Carlo distributions did not mimic this behavior because the vertex position of MC events was always known exactly. Fitting the distributions in the 'non-tail' region yielded purities differing by only $\sim$.1%, demonstrating that the tails were not interfering in the purity determination.

To be accurate, this technique required that each point in the data distributions be statistically significant, so that the fit would be performed to a statistically significant distribution. This was not the case in some of the photon plus two jet events. However, since it was not possible to analytically extract an expression for the error on the purity measurement that took into account the statistical significance of the data used in the fit, the errors that were obtained from the fit were used consistently.

Appendix B contains the results of all the fits for the photon plus one jet case where $E_T^{jet}{}_{min} = 25\text{GeV}$.

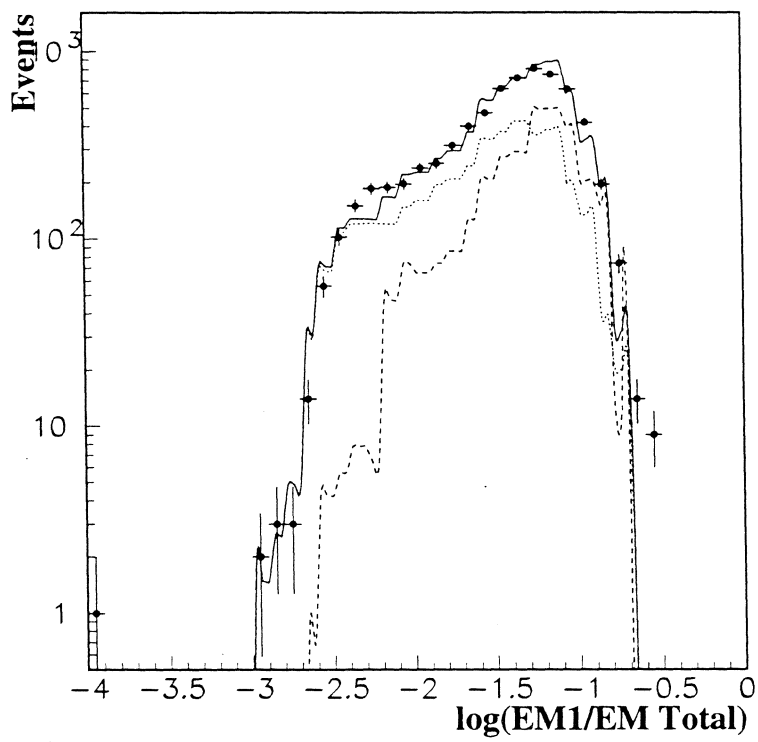

Figure 3.6: Fit of MC to Data. The data points are shown with statistical errors. The dashed line is the fit contribution from MC photons, the dotted line is the same for jets, and the solid line is the best fit of the sum of the two MC distributions. The data shown consists of photon candidates with $30 < E_T^\gamma < 40$ GeV. The purity for this data was determined as $P = .55 \pm .02$. The data was used to normalize this plot. The right side tail of the data distribution was not modeled well by the MC.

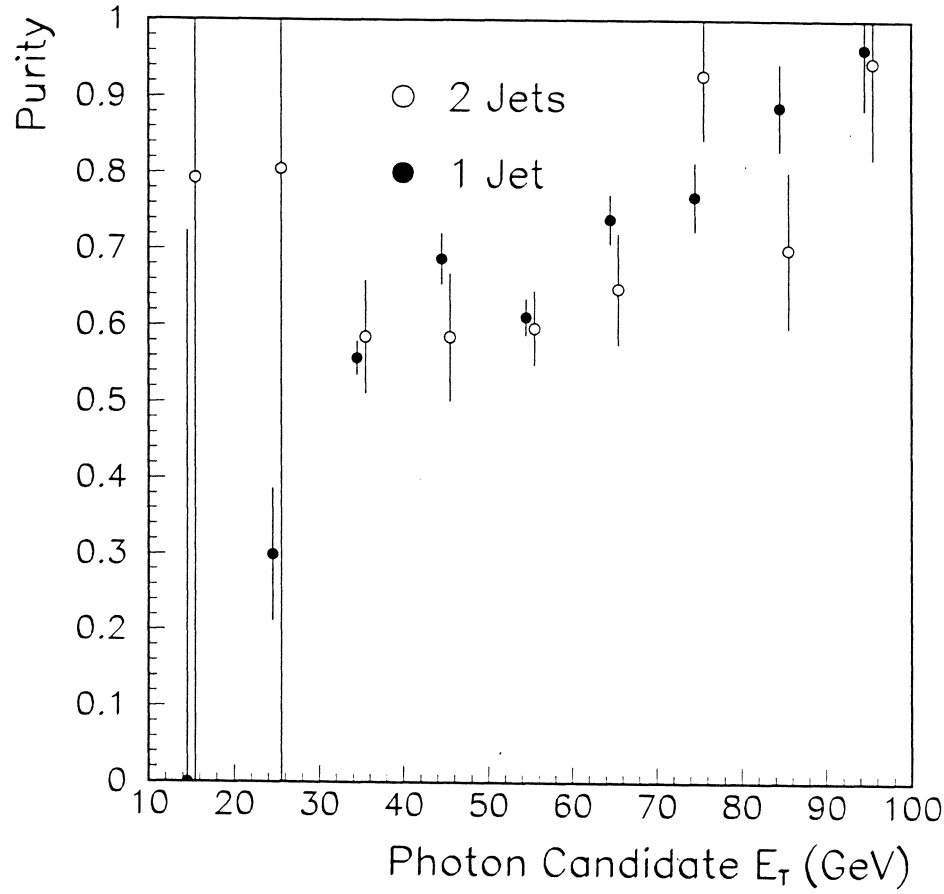

Figure 3.7: Measured Photon Candidate Purity as a Function of E_T^γ. Purities are plotted with systematic errors for the 1 and 2 jet cases. The errors on the 10-20 and 20-30 GeV points for the 2 jet case were not calculable due to low statistics in the data sample.

CHAPTER 4
MONTE CARLO

Simulated photons and neutral mesons were needed for efficiency studies in kinematic regions where data were not available. These were used to test the trigger efficiencies and to make the distributions of local variables used in photon background discrimination. These events were generated by Pythia [35], and the particles near ($R < 1.0$) the photon or neutral meson were passed to the time consuming Geant [36] detector simulation program. In both cases, to add realistic detector effects, real zero-bias data events were added to the simulation output. The resulting Monte-Carlo events were processed by the standard DØ reconstruction program.

4.1 Event Generation

The Pythia event generator was used to get the kinematics of both the direct photon signal and QCD background. Pythia is a leading order event generator that includes higher order effects through a parton shower algorithm. As such it has only tree-level $2 \rightarrow 2$ processes explicitly included. For direct photons, the Compton and Annihilation processes are used, and for QCD background $[qq, qg, gg] \rightarrow [qq, qg, gg]$ are used. Initial state radiation is added after the hard scattering is evaluated using the backward evolution algorithm [37]. Higher order branching of the primary partons is handled with a parton shower algorithm [38] and the string fragmentation algorithm [39]. All partons are hadronized resulting in a list of final state particle 4-vectors. For these analysis, π^0 and η mesons were inhibited in their decays, which simplified the implementation of the filter algorithm.

To reduce the number of background events passed to the detector simulator, an algorithm was implemented to pass only jet events with isolated electromagnetic clusters. This was done to ensure that the majority of subsequently reconstructed events would pass the photon candidate selection cuts. First, an E_T-ordered list of all π^0 and η mesons with $E_T > 5GeV$ was made. These 'seeds' were used as the center of $R = 0.2$ and 0.4 cones in $\eta - \phi$ space. All other particle energies within these cones were added for each event. A cluster energy was taken to be the energy in the $R = 0.2$ cone, and the isolation energy was taken as the energy in the $R = 0.2 - 0.4$ annulus. The seed was rejected if the associated cluster had less than 10 GeV or the isolation cone energy was greater than 2 GeV of E_T. The cluster was also required to have at least 60% of its parent parton's energy and to have no charged particles in the $R = 0.2$ cone. These seed rejection cuts were imposed to mimic the online trigger which had similar requirements. The fraction of events passing these selection criteria varied with E_T from $10^{-3} - 10^{-4}$.

4.2 Detector Simulation

The Geant3 package [36] was used as the basis for the DØ detector simulation. The photon simulations used a detailed description of the calorimeter, which included individual Uranium plates, G10 readout and signal boards, and liquid Argon gaps. In addition, the steel supports and cryostats were included in the geometric model. The Geant package then performed the ray tracing between various detector volumes and simulated the different energy loss mechanisms using MC techniques. To obtain a good simulation of electromagnetic showers, it was necessary to trace the electrons and photons until their energies dropped below 10 KeV. Tracing was stopped at this point, and the particle's energy was deposited at a single point.

4.3 Noise and Pileup Effects

The Geant program only simulated the physical processes of energy deposition. Rather than attempt to describe the complexities of ions drifting in Argon, and the geometry dependant effects of amplifiers, cables and digitization hardware, these effects were measured together using a special trigger that required only a bunch crossing to fire. These zero-bias events were recorded at five different luminosities and literally added to the simulated data channel-by-channel. These triggers also captured the electronic effects of previous bunch crossings and the effects of multiple interactions in one bunch crossing.

For the events generated for the purity determination, each Pythia/Geant event was used about 10 times by adding a different zero-bias event to a single Pythia/Geant event. This smoothed the MC distributions without significantly affecting the statistical independance of the local calorimeter variables (EM_1, EM_{Total} *etc...*) used in the analysis.

4.4 Comparison of Monte Carlo and Data

The purity determination of photon candidates in this analysis relied heavily on the accuracy of MC simulations. To test how accurately the MC events reproduced actual results, a sample of MC W$\rightarrow$ $e + \bar{\nu}_e$ events was generated and compared to data. Since it was not possible to tell on an event by event basis whether a photon candidate was actually a photon or a highly electromagnetic jet, no sample of real photons was available to compare with the Monte Carlo; however, electrons from W decays were simple to identify. A sample of these events was selected from the data, and another sample generated in MC. Both data and MC electrons were required to pass all standard photon candidate selection cuts except that a CDC

Table 4.1: $W \rightarrow e\nu$ Distribution Centroids for Data and Monte Carlo

Electrons $30 < E_T^e < 40$ GeV	Data	Monte Carlo	Kolmogorov Likelihood
Discriminant Variable $\log(EM1/EM_{Total})$	-1.23 ± 0.01	-1.22 ± 0.01	0.947
Isolation E_T	.88 ± 0.02	.70 ± 0.02	0.0
Cluster Electromagnetic Fraction	0.9924 ± 0.0003	0.9931 ± 0.0003	0.41244
Shower Shape χ^2	24.4 ± .8	23.5 ± .7	0.20325

track was required and the event's $\not\!\!E_T$ was required to be greater than 20 GeV. Then the data and MC distributions of several variables were compared. Figure 4.1 show distributions for electrons with $30 < E_T^e < 40$ GeV. Table 4.1 lists the centers of the distributions, the uncertainty on them, and the results of a Kolmogorov likelihood test. The agreement between the MC and data distributions of the discriminant variable, the shower shape variable χ^2, and the cluster electromagnetic fraction was good; however, the agreement between the data and MC isolation E_T was not as good, since some of the data were taken at high luminosities but the MC only had calorimeter noise added from one minimum bias run at a luminosity of $5 \times 10^{30}/(s\,cm^2)$. Since the noise had contributions from both constant (Uranium noise and electronics) and luminosity dependant (underlying events and multiple interactions) sources which could not be deconvoluted, it was not appropriate to simply add two zero bias events to the MC event in an attempt to model the data. In general, the higher the luminosity, the larger the isolation E_T contribution was from underlying events and multiple interactions. However, the excellent agreement between the data and MC discriminant variable distributions as determined by a Kolmogorov Likelihood test demonstrates the soundness of the MC, and the choice of this variable as a discriminant.

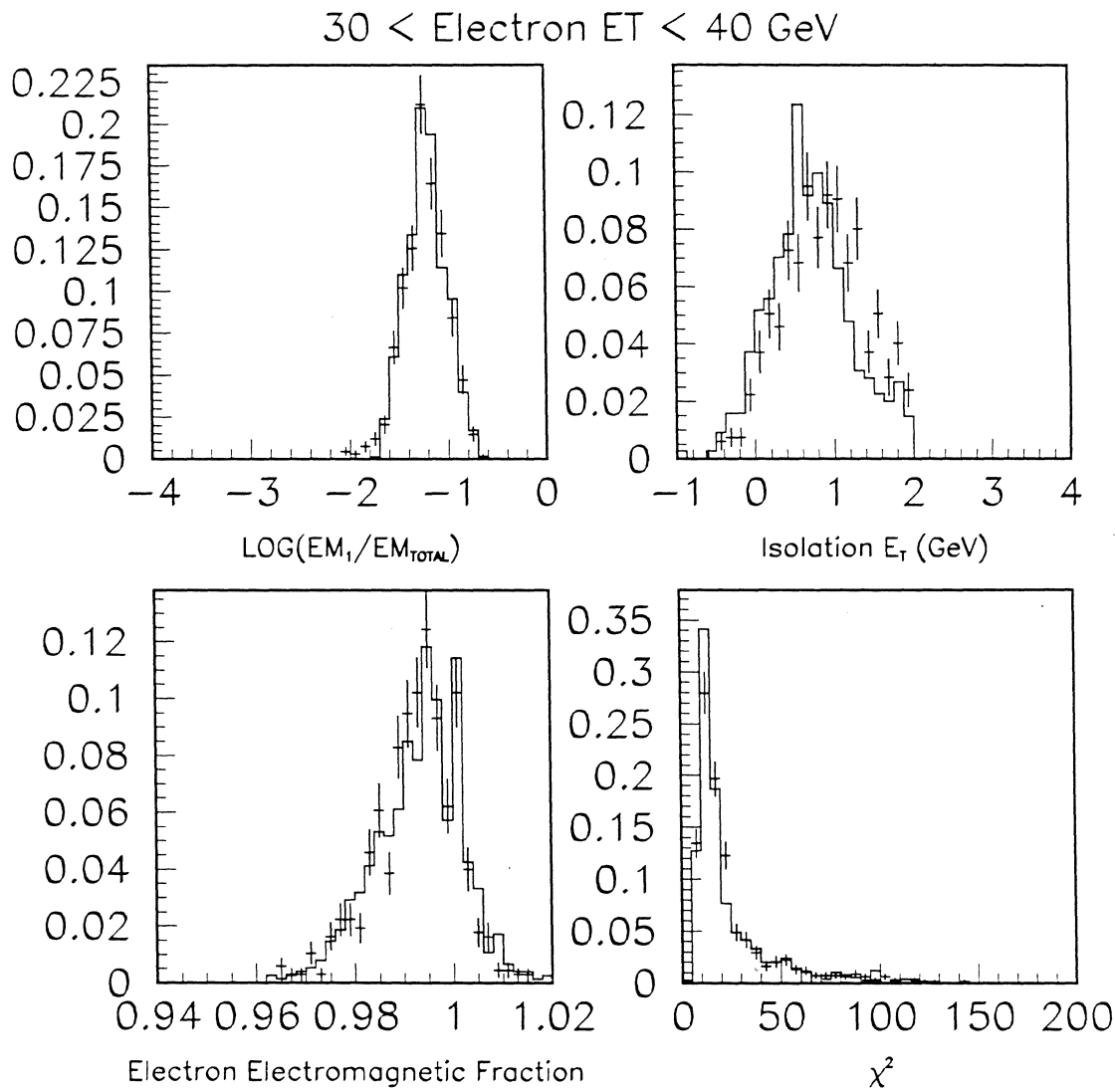

Figure 4.1: Distributions of the discriminant variable, the isolation E_T, the cluster electromagnetic fraction and the shower shape variable χ^2 for Data and MC Electrons from W$\rightarrow e + \bar{\nu}_e$ events. The MC are shown by the solid histogram, the data by crosses that give the statistical error on each point. The differences between the data and theory plots of the isolation E_T distributions are due to the fact that the MC had zero bias event noise added to it that was taken at medium luminosities, while the data were taken at all luminosities.

CHAPTER 5
COMPARISON OF THEORY AND DATA

5.1 Theoretical Calculations

The leading order calculation of direct photon production can predict the kinematics of photon plus one jet events using the $2 \rightarrow 2$ tree-level Compton and Annihilation Feynman graphs shown in Chapter 1. The partonic cross sections are given by:

$$\frac{d\sigma}{dt} = \frac{\pi\alpha\alpha_s e^2}{3s^2}\left(\frac{u}{s} + \frac{s}{u}\right)$$

and

$$\frac{d\sigma}{dt} = \frac{\pi\alpha\alpha_s e^2 8}{9s^2}\left(\frac{u}{t} + \frac{t}{u}\right)$$

where the strong running coupling $\alpha_s(Q^2)$ is

$$\alpha_s(Q^2) = \frac{12\pi}{(33 - 2n_f)\, ln(Q^2/\Lambda^2)}$$

and the relativistically invariant Mandelstam variables s,t, and u are defined as

$$s = (P_1 + P_2)^2$$

$$t = (P_2 - P_4)^2 = (P_1 - P_3)^2$$

$$u = (P_1 - P_4)^2 = (P_2 - P_3)^2$$

where P_i are the four momenta of the incoming $(i = 1,2)$ and outgoing $(i = 3,4)$ partons or photon. The quantity Q^2 is the 'renormalization scale' of the interaction, and is usually chosen to be $Q^2 = C\, E_T^2$ where $.5 < C < 2$, where the E_T is that of the highest E_T body in the event. The renormalization scale is ultimately due to the fact that the perturbative expansion of the cross section is truncated at a fixed

order. If the expansion were not truncated there would be no ambiguity and no scale choice would be necessary. In addition to the Compton and Annihilation processes, a complete LO calculation must also include the effect of photon bremsstrahlung off quarks in dijet events. This process appears to be of order $\alpha_s^2\alpha$; however, since bremsstrahlung is a nearly collinear process, simple vertex counting is not sufficient. One procedure to account for this process is to factorize the hard scattering from the photon emission, which is then treated separately by a phenomenological fragmentation function that gives the probability of a photon receiving a certain fraction (z) of the parton's momentum. Integration of the quantum mechanical bremsstrahlung formula [40] gives rise to a factor of order $\log(Q/\Lambda)$. This logarithm combined with electromagnetic coupling produces a term of order α/α_s, which yields a cross section of leading order ($\alpha\alpha_s$). At Tevatron energies, where the multi-jet cross section is $\sim 10^3$ larger than that for direct photons, it is necessary to impose an isolation cut around the direct photons to reduce the hadronic background to manageable levels. Theoretically this is equivalent to integrating the fragmentation function over the range where the photon carries a large fraction of the parent parton momentum. The convolution of the $\sim E_T^{-4}$ dependance of hard scattering cross sections with the vanishing probability of a parton giving almost all of its energy to a photon, results in a cross section contribution which is significant only at low E_T^γ.

The theory does not make any predictions about final states involving more than two jets. Such events do occur however, and if one of them contains a jet that fragments into a photon, the result would be an enhancement in the cross section, provided that the other jets satisfied the cut on ${E_T^{jet}}_{min}$. The difficulty in accounting for such events arises from the fact that some unknown fraction will pass the photon candidate selection cuts, particularly the cut on isolation E_T. This contribution is not calculable since, as mentioned above, an integration is performed. This obliterates any information about accompanying particles. As a result, particularly at

low E_T, there can be contributions to the measured cross section which are not accounted for in the theory.

A next to leading logarithm calculation exists [41] which allows a second jet in the final state; however, at NLO there are also singularities which occur when any of the initial or final state partons become collinear. Also, soft singularities arise in the $2 \rightarrow 3$ LO process when one of the outgoing partons becomes soft (has very little energy); however, the contribution of one-loop graphs ($2 \rightarrow 2$ processes with an internal gluon loop) will cancel them in the full calculation. Several techniques are used to handle these singularities. Collinear singularities associated with the initial state partons are dealt with by absorbing such low momentum transfer processes into the parton distribution functions (*pdf*). These parameterizations give the probability that a particular parton will have a fraction (z) of the protons's (antiproton's) momentum. The calculation by Baer, Ohnemus and Owens uses the so-called $\overline{MS}$ scheme to factorize the cross section calculation into perturbative and nonperturbative parton level processes.

The analytic techniques which allow for the cancellation of soft and collinear singularities in the $2 \rightarrow 3$ processes are performed and the resulting nonsingular cross section contribution is added to the $2 \rightarrow 2$ cross section. Away from singular kinematic regions, the $2 \rightarrow 2$ and $2 \rightarrow 3$ cross sections are evaluated by Monte Carlo integration. The analytic and Monte Carlo techniques are tied together by two cutoff parameters which define the regions of phase space where each technique is employed. The cutoff parameters, which define soft and collinear regions, appear in the terms for the soft corrections and modify the bremsstrahlung contribution, which also must be used in the NLO calculation to correctly account for the isolation cut. As long as the cutoffs are small, they do not interfere with the experimentally driven cuts and their exact values do not matter.

The end result is a program which produces kinematic configurations and a weight for three types of events: $2 \rightarrow 2$, $2 \rightarrow 3$, and $2 \rightarrow 2$+bremsstrahlung. The photon plus one and two jet cross sections cannot be directly calculated from these independently since this would not produce observable quantities. In fact, the weights of the $2 \rightarrow 2$ processes at NLO can be negative. Experimentally, jets could not be measured with good precision at high rapidities, so they were counted only if $|\eta^{jet}| < 2.5$. Also, low E_T jets were not well measured so a cutoff of $E_T^{jet} > 25\,GeV$ was used. Since fully fragmented and hadronized jets are of finite size, it is not possible to resolve jets that are close together. In fact the use of fixed-cone jet definition algorithms inhibits this. For this reason, if a theoretical event has jets that are closer than $R = 0.7$, the two jets are added vectorially into a single jet. Events of this type then are counted as single jet events, resulting in a positive contribution to the photon plus one jet cross section which compensates for the negative, one-loop NLO $2 \rightarrow 2$ contributions.

Only the photon plus one jet cross section is truly NLO, since there are no radiative (one loop) corrections to the photon plus two jets cross section. As such, the $\sigma_{\gamma+2jets}$ cross section should exhibit sensitivity to the choices of factorization and renormalization scale. This relatively large degree of sensitivity to the choice of scale is not found in the NLO calculation due to the partial cancellation of scale dependant terms in the NLO partonic cross section and parton distribution functions. Figure 5.1 shows the two differential cross sections as a function of Q^2 choices. The NLO calculation shows $\sim 5\%$ change, while the LO calculation shifts $\pm 15\%$.

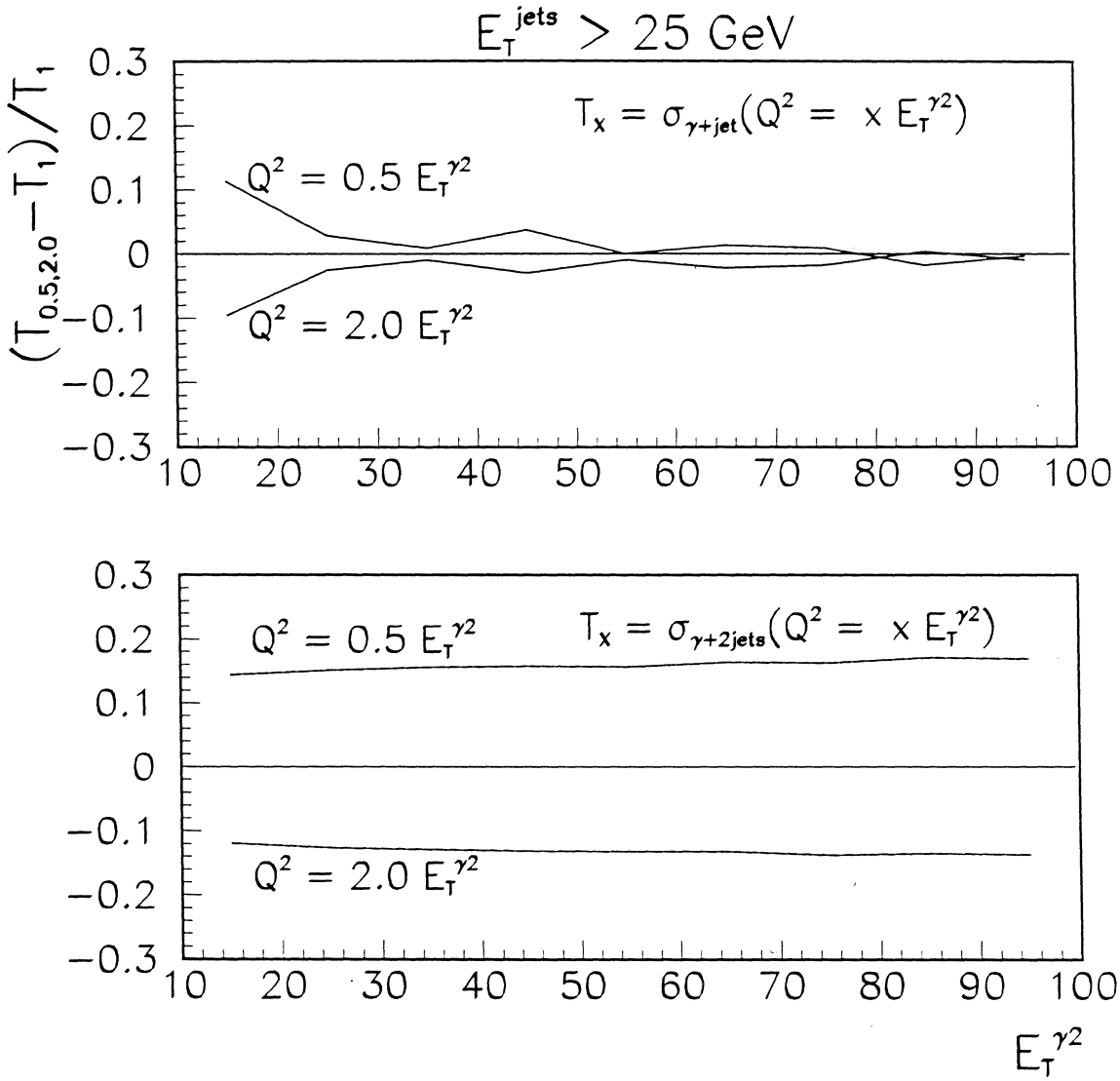

Figure 5.1: Dependance of the Differential Cross Sections on $Q^2 = (0.5\,, 1.0\,, 2.0)E_T^2$. The dependance is shown in (data-theory)/theory form, where the data is replaced by theory with choices of $Q^2 = .5$ and $2.0{E_T}^2$. As expected, the LO $\sigma_{\gamma+2jets}$ cross section exhibits much more dependency on the choice. The fluctuations in the $\sigma_{\gamma+jet}$ cross section are statistical in nature.

5.2 The Measured Exclusive Isolated Photon Cross Sections

In this measurement, an event must have had one and only one jet of an E_T greater than ${E_T^{jet}}_{min}$ to have been counted in $\sigma_{\gamma+jet}$ and two and only two jets of an E_T greater than ${E_T^{jet}}_{min}$ to have been counted in $\sigma_{\gamma+2jets}$. Theoretically, these cuts defined two regions of integration over jet E_T, one greater than the cut, and one less than the cut. This exclusive treatment of the jets allowed for a comparison to be made between the data and theory, since the exact NLO and LO theoretical calculations used here were limited to at most two jets above the E_T cut.

Data points with a fractional error >100% or a null purity were not shown. Figure 5.2 shows the differential cross sections as a function of E_T^γ, given a particular value of ${E_T^{jet}}_{min}$. Figure 5.3 shows the same data in (data-theory)/theory form. Figure 5.4 is a plot of the data for ${E_T^{jet}}_{min} = 25$ GeV. The photon plus one jet cross section is clearly in agreement with theory. The deficiency of the lowest E_T^γ point in the ${E_T^{jet}}_{min} = 25$ GeV plot can be explained as follows. First, most of the photons in the bin have E_T^γ close to 20 GeV, since the cross section drops exponentially with increasing E_T^γ. Second, all jets $E_T^{jet} > 25$ GeV can contribute to this bin, and although they too are concentrated towards 25 GeV in E_T^{jet}, some higher E_T jets are present. From conservation of transverse momentum, the final state bodies's transverse momentum vectors must sum to zero[1], this means that if an event has one high E_T jet 'balanced' by a 'low' E_T photon roughly opposite it in ϕ, there must be another jet in the same ϕ hemisphere as the photon in order to conserve momentum. This accompanying jet, even though it has less than 25 GeV of E_T will occasionally deposit sufficient energy close enough to the photon to cause it to fail the experimental isolation cut, thereby reducing the measured cross section for that bin. With higher E_T photons and jets, the impact of this effect will be sharply curtailed by the exponentially falling cross section.

[1]This is only approximately true, but holds for the argument being made.

The photon plus two jet cross section is in good agreement with the theoretical predictions when the E_T^{jet} cut is set no larger than 45 GeV. The small number of events ($\sim$ 20 / photon bin) with two jets $E_T^{jet} > 45$ GeV was insufficient to guaranty the accuracy of the purity determination procedure. Given this statistical limitation, the agreement is not inconsistent with the theory, even at large ${E_T^{jet}}_{min}$, considering that the errors are systematically underestimated there. More data will have to be collected, however, to make a precision measurement of this region of phase space.

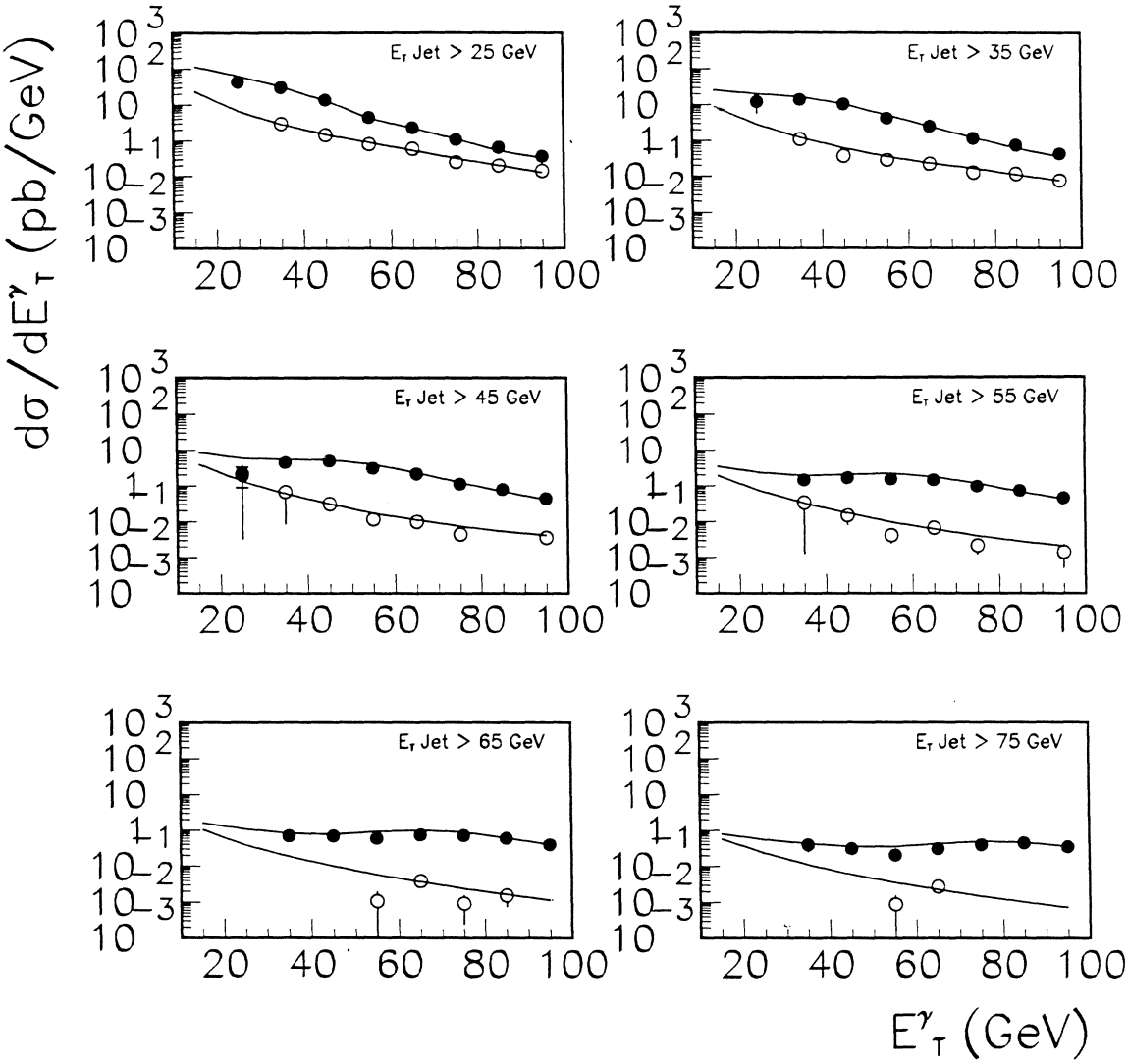

Figure 5.2: The Differential Cross Sections $\frac{d\sigma_{\gamma+jet}}{dE_T^\gamma}$ and $\frac{d\sigma_{\gamma+2jets}}{dE_T^\gamma}$ given $E_T^{jet(s)} > 25$ through 75 GeV. The closed and open dots are data for the one and two jet cases respectively. The upper and lower lines are theoretical predictions for the one and two jet cases respectively made using CTEQ4M *pdf*s where $Q^2 = {E_T}^2$.

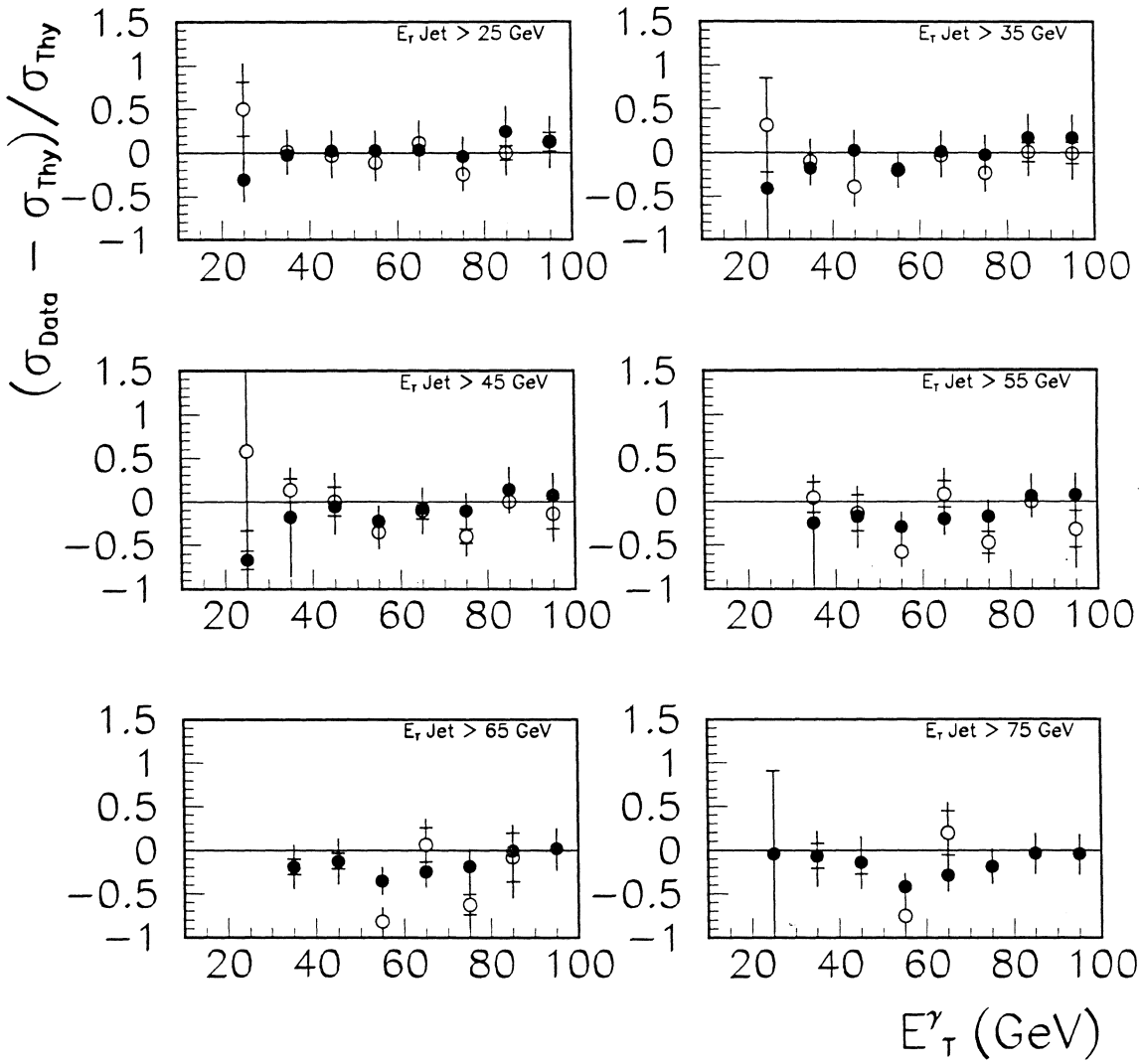

Figure 5.3: The Differential Cross Sections $\frac{d\sigma_{\gamma+jet}}{dE_T^{\gamma}}$ and $\frac{d\sigma_{\gamma+2jets}}{dE_T^{\gamma}}$ given $E_T^{jet(s)} > 25$ through 85 GeV plotted in (data-theory)/theory form. The line shows theoretical predictions for the one and two jet cases (closed and open dots respectively) made using CTEQ4M *pdf*s where $Q^2 = {E_T}^2$. The statistical errors are given by the tic marks and the systematic errors are shown by the left and right slanted regions for the one and two jet cases respectively.

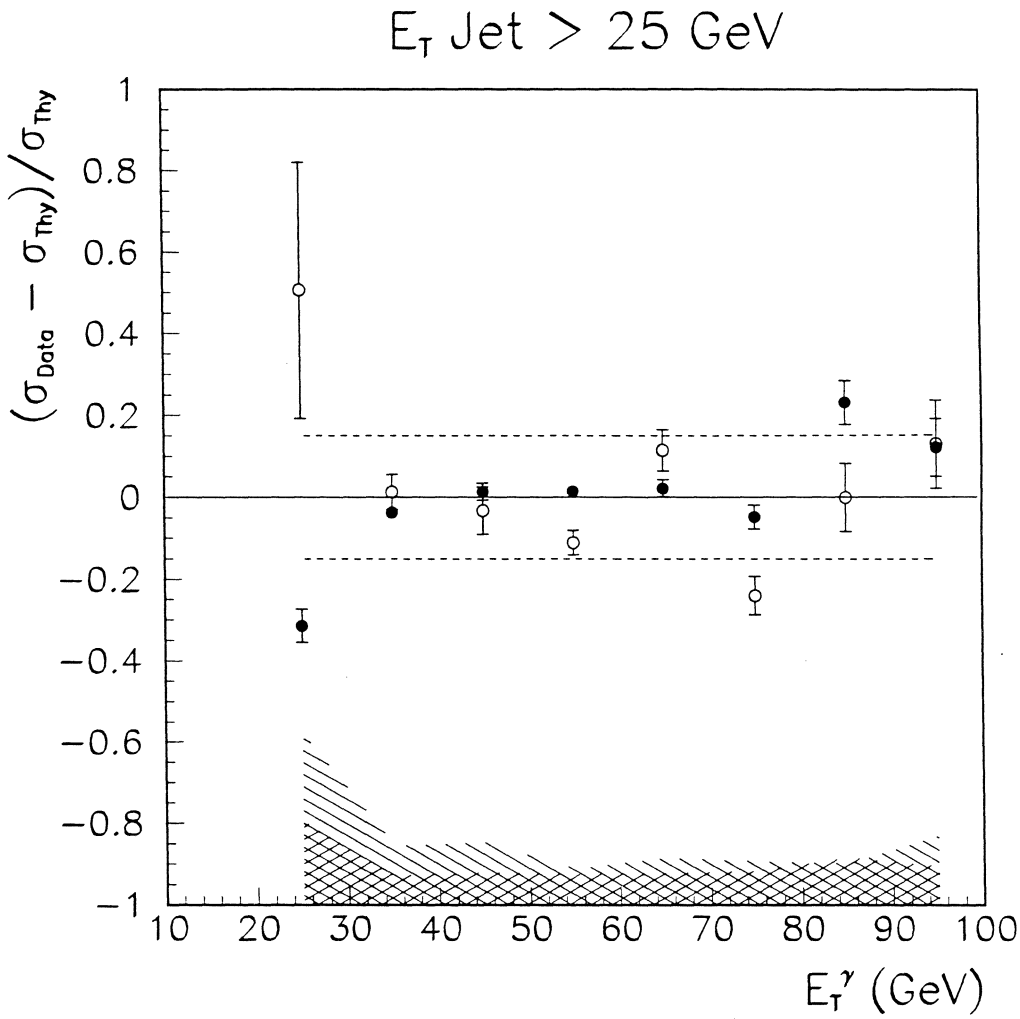

Figure 5.4: The Differential Cross Sections $\frac{d\sigma_{\gamma+jet}}{dE_T^{\gamma}}$ and $\frac{d\sigma_{\gamma+2jets}}{dE_T^{\gamma}}$ given $E_T^{jet(s)} > 25$ GeV plotted in (data-theory)/theory form. The solid line is theoretical predictions for both the one and two jet cases (closed and open dots respectively) made using CTEQ4M *pdf*s where $Q^2 = {E_T}^2$. The statistical errors are given for each point by the tic marks, and the left and right slanted regions give the scaled systematic errors for the one and two jet cases respectively. The upper and lower dotted lines represent theoretical predictions made choosing $Q^2 = 0.5{E_T}^2$ and $Q^2 = 2.0{E_T}^2$ respectively.

5.2.1 Errors on the Measurement

The systematic errors consisted of the quadratic sum of the errors on the luminosity, fiducial cut efficiency, jet selection cut efficiency, $\not{E}_T$ cut efficiency, photon candidate selection cut efficiencies, and the photon purity. These are all highly correlated.

Although the efficiencies of the photon candidate selection cuts were measured and their errors accounted for, the cuts themselves were not deduced from an underlying principle. They were chosen, based on previous experience, in a fashion that retained most photons while rejecting the majority of multi-photon background events. The cross sections were functions of the photon candidate selection cuts C_{iso},C_{emf}, and C_{χ^2} where the C stands for the various cut values, and their respective cut efficiencies as calculated from MC photons ϵ_{iso},ϵ_{emf}, and ϵ_{χ^2}. In general this means

$$\sigma(C_{iso}, C_{emf}, C_{\chi^2}) \propto \frac{N(C_{iso}, C_{emf}, C_{\chi^2})P(C_{iso}, C_{emf}, C_{\chi^2})}{\epsilon_{iso}\epsilon_{emf}\epsilon_{\chi^2}}.$$

In order to determine the dependance of the cross section measurement on the photon candidate selection cut values, they were each varied independently by a significant amount, and the cross section was re-evaluated. No statistically significant dependance was observed, though in some instances the 'tight' cuts rejected all the events, and the 'loose' cuts allowed in too much background, causing a null purity. The differences in the recalculated cross sections typically differed from the original cross sections by 10% or less, which was well within the calculated systematic error. Figures A.1 through A.3 show the calculated cross sections, for $E_T^{jet}{}_{min} >$ 25 GeV, as the selection cuts are varied. These plots show the nominal cut choice, the two variations of selection cut, and the overall χ^2 / $d.o.f.$ for the one and two jet cases for each variation. In all cases, no overall statistically significant dependance is observed. This is reflected in the small values of χ^2 / $d.o.f.$.

Table 5.1: Photon Candidate Selection Cut Variations

Variable	Loose Cut	Nominal Cut	Tight Cut
Electromagnetic Fraction C_{emf}	$> 94\%$	$> 96\%$	$> 98\%$
Shower Shape χ^2 C_{χ^2}	< 200	< 150	< 100
Isolation E_T (GeV) C_{iso}	< 2.5	< 2.0	< 1.5

5.2.2 Uncertainty Due to Jet Energy Scale

An additional source of error was the uncertainty in the measurement of jet energies. The analysis was preformed using the nominal jet energy scale[2] and was repeated using jet energies that were one standard deviation high and low to reflect fluctuations in jet E_T measurement. Figure A.4 shows the ${E_T^{jets}}_{min} = 25$ GeV case and the resulting χ^2 values for both energy scale variations. No statistically significant difference was observed. Tables 5.2.2 and 5.2.2 contain the factors that went into the cross section calculation for $\sigma_{\gamma+jet}$ and $\sigma_{\gamma+2jets}$ respectively, on a point by point basis, where ${E_T^{Jet(s)}}_{min} = 25$ GeV.

[2]The 5th version of the jet energy scale correction package CAFIX was used.

E_T^γ	N	P	A	ϵ_{sel}	ϵ_{met}	$\mathcal{L}$	$\sigma_{\gamma+jet}$ (pb)
15	44.± 6.63	0.00± 0.723	-	-	-	-	-
25	283.±16.82	0.30± 0.087	.753±.025	.849±.002	.996±.004	0.210±0.013	43.727±13.058
35	6823.±82.60	0.56± 0.022	.744±.005	.868±.003	.972±.002	13.450±0.81	31.073± 2.283
45	2432.±49.32	0.69± 0.034	.744±.009	.875±.003	.963±.004	13.450±0.81	13.678± 1.083
55	5621.±74.97	0.61± 0.024	.746±.006	.878±.004	.936±.003	87.31±5.24	4.433± 0.324
65	2380.±48.79	0.74± 0.032	.746±.009	.883±.004	.915±.005	87.31±5.24	2.310± 0.177
75	1057.±32.51	0.77± 0.045	.746±.013	.881±.004	.902±.009	87.31±5.24	1.085± 0.095
85	521.±22.83	0.89± 0.057	.746±.019	.875±.004	.871±.014	87.31±5.24	0.643± 0.060
95	257.±16.03	0.96± 0.080	.746±.026	.887±.004	.824±.022	87.31±5.24	0.359± 0.035

Table 5.2: Summary Table of Cross Section Parameters for $\sigma_{\gamma+jet}$. The quantities $\Delta\eta = 1.8$, $\Delta E_T = 10$ GeV, $\epsilon_{trk} = .82 \pm .009$, and $\epsilon_{jet} = .969 \pm .003$ were constant at all E_T^γ. Statistical errors are shown for N, Systematic errors only for the rest. The purity calculation for the $E_T^\gamma = 15$ GeV bin was null, and hence was not shown.

E_T^γ	N	P	A	ϵ_{sel}	ϵ_{met}	$\mathcal{L}$	$\sigma_{\gamma+2jets}$(pb)
15	13.± 3.61	$\mathcal{A}$	-	-	-	-	-
25	23.± 4.80	$\mathcal{A}$	-	-	-	-	-
35	574.±23.96	0.58± 0.074	.744±.018	.868±.003	.921±.011	13.450±0.81	2.987± 0.427
45	276.±16.61	0.60± 0.083	.744±.026	.875±.003	.911±.016	13.450±0.81	1.470± 0.231
55	912.±30.20	0.65± 0.049	.746±.014	.878±.004	.921±.009	87.31±5.24	0.800± 0.079
65	495.±22.25	0.93± 0.073	.746±.019	.883±.004	.929±.011	87.31±5.24	0.613± 0.063
75	262.±16.19	0.70± 0.084	.746±.026	.881±.004	.919±.016	87.31±5.24	0.248± 0.035
85	147.±12.12	0.95± 0.102	.746±.035	.875±.004	.875±.026	87.31±5.24	0.199± 0.024
95	112.±10.58	0.89± 0.126	.746±.040	.887±.004	.882±.029	87.31±5.24	0.140± 0.022

Table 5.3: Summary Table of Cross Section Parameters for $\sigma_{\gamma+2jets}$. The quantities $\Delta\eta = 1.8$, $\Delta E_T = 10$ GeV, $\epsilon_{trk} = .82 \pm .009$, and $\epsilon_{jets} = .939 \pm .004$ were constant at all E_T^γ. Statistical errors are shown for N, Systematic errors only for the rest. ($\mathcal{A}$) The purity calculation for the $E_T^\gamma = 15$ and 25 GeV bins was not reliable due to low statistics.

CHAPTER 6
SUMMARY AND CONCLUSIONS

The results presented in this dissertation represent the first comparison between data and theory for direct photons produced with one and two jets at the Tevatron. The D0 detector has superb energy resolution and segmentation in the calorimeter. In addition to the fine lateral segmentation, the longitudinal segmentation allowed the differentiation between direct photons and photons due to π^0 or η meson decays. The purity of the direct photons was determined from the fractional conversion probability of the gamma particles in the first layer of the electromagnetic calorimeter, as π^0 or η meson decays have two photons each and the probability for one of them to convert in the first calorimeter layer is twice that of a single direct photon.

The kinematic region studied for photons was eta < 0.9, $E_T^\gamma > 20$ GeV and for jets of pseudorapidity < 2.5 and $E_T > 25$ GeV. The choice of these limits was to allow for the clear identification of photons and jets. After all the cuts for the photons, the purity of direct photons varied from about 30% at E_T^γ of 25 GeV to over 90% for E_T^γ greater than 85 GeV. The jet minimum E_T is required to ensure high efficiency in offline reconstruction. A total of 19,374 direct photon candidate events were identified with one jet and 2,801 direct photon candidate events with two jets. The overall purity estimate is $63.3 \pm 4.7\%$.

The direct photon plus one jet cross section was compared to the next to the leading (NLO) order QCD calculation using the CTEQ4M parton distribution functions (pdf's). The agreement is excellent. Table 6.1 shows the $\chi^2/d.o.f.$ on the data where $\chi^2 = \sum_{E_T^\gamma}(\frac{\sigma_{Exp}-\sigma_{Thy}}{\Delta\sigma_{Exp}})^2$. The result of χ^2 on the order of or less than 1 for all the different $E_T^{jet}{}_{min}$ cuts indicates that the theory is in good agreement with the photon

Table 6.1: Table of $\chi^2/d.o.f.$ for Each Differential Cross Section

${E_T^{jet}}_{min}$	$\chi^2/d.o.f.$ for $\sigma_{\gamma+jet}$	$\chi^2/d.o.f.$ for $\sigma_{\gamma+2jets}$
25	.307	.32
35	.55	.72
45	.93	1.17
55	1.03	2.92
65	1.23	7.24
75	1.51	6.83

plus one jet data in all kinematic regions where the background subtraction procedure was successful. The direct photon plus two jets cross section was compared to lowest order QCD predictions, again made using the CTEQ4M pdf's, and the agreement is also very good. The direct photon plus two jets cross section was best described by LO QCD when $E_T^{jets} > 25, 35$, and 45 GeV. The purity calculation was decreasingly reliable at higher ${E_T^{jets}}_{min}$ cuts, due to the rapidly decreasing statistics which limited the reliability of the purity calculation. The conclusion is that the Standard Model calculations describe the data very well.

APPENDIX A

THE SYSTEMATIC DEPENDANCE OF THE CROSS SECTION MEASUREMENTS ON THE PHOTON CANDIDATE SELECTION CUTS

The following plots show the results of varying the photon candidate selection cuts, and the cross section calculations. They also show the dependance of the cross section on the jet energy scale. In all cases, no statistically significant dependance is seen, as the differences in the results are less than the systematic errors.

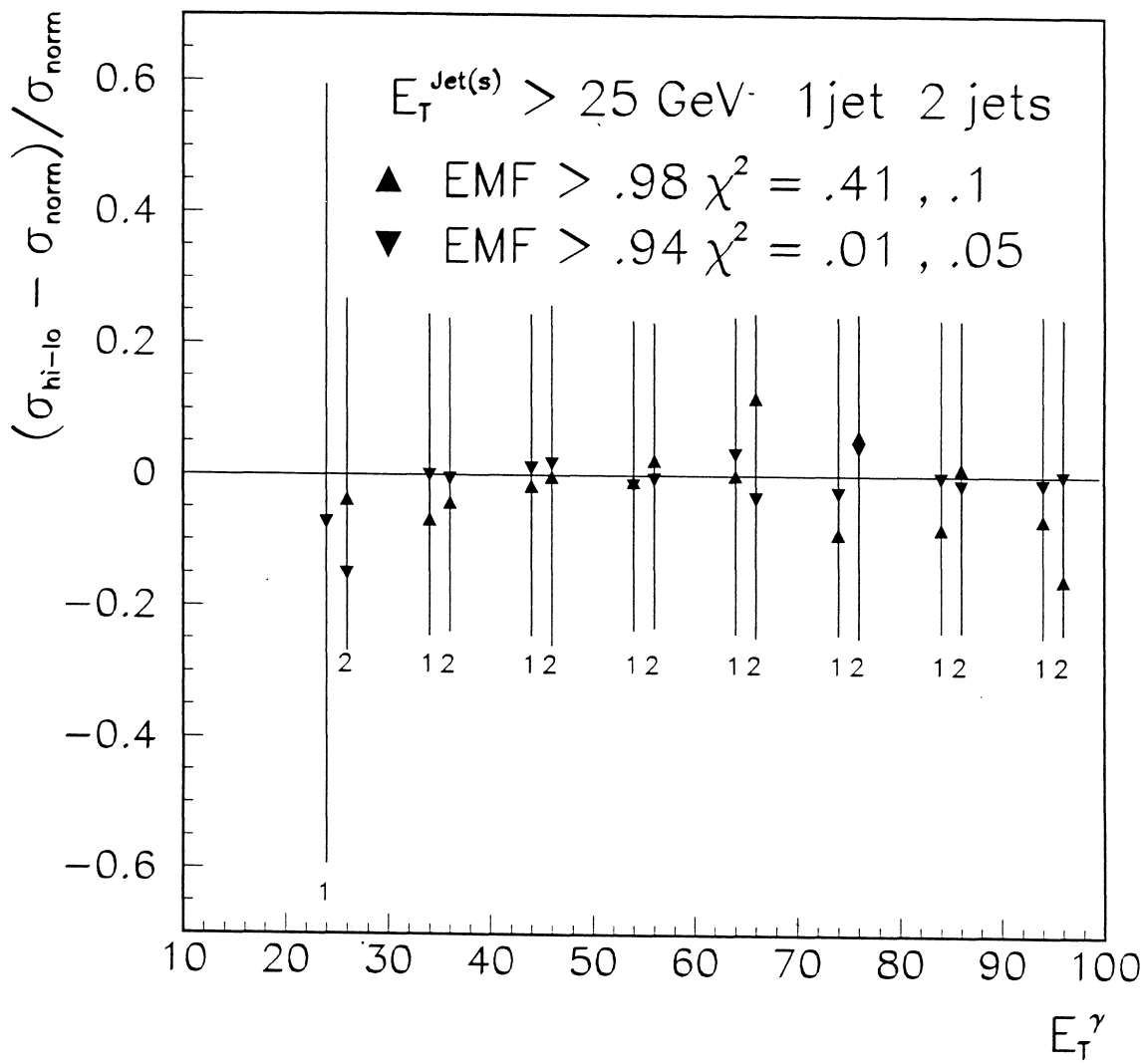

Figure A.1: Dependance of the Cross Sections on the Electromagnetic Fraction Cut. The axis represents the cross sections as calculated with the nominal cuts, the up and down arrows show the respective 'tight' and 'loose' cuts. The χ^2 / *d.o.f.* is then shown for each cut, and both the one and two jet cross sections. The error bars show the systematic errors for the nominal cut choice.The numbers underneath each error bar distinguish the one and two jet cases respectively.

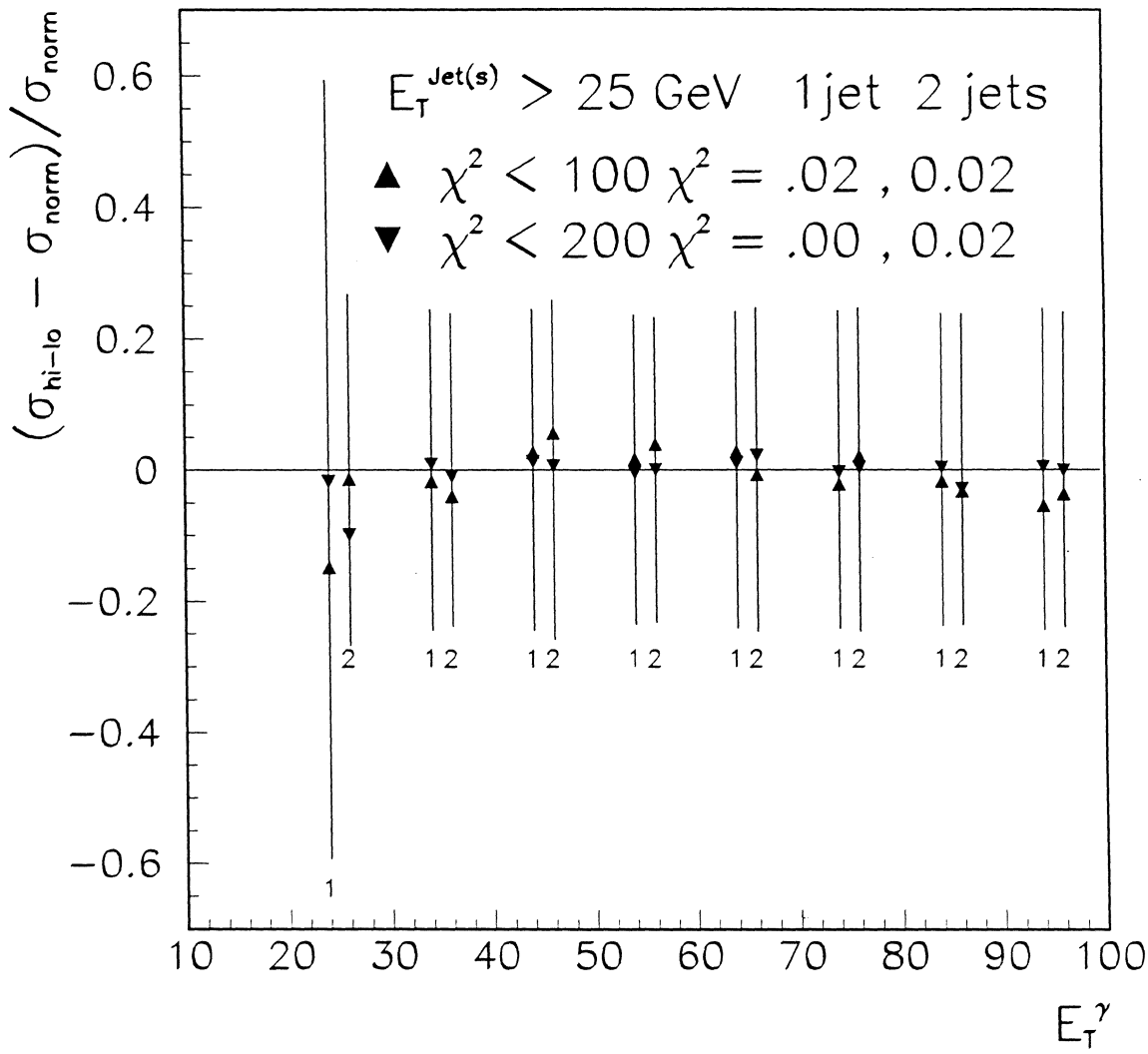

Figure A.2: Dependance of the Cross Sections on the Shower Shape Cut. The axis represents the cross sections as calculated with the nominal cuts, the up and down arrows show the respective 'tight' and 'loose' cuts. The χ^2 / *d.o.f.* is then shown for each cut, and both the one and two jet cross sections. The error bars show the systematic errors for the nominal cut choice. The numbers underneath each error bar distinguish the one and two jet cases respectively

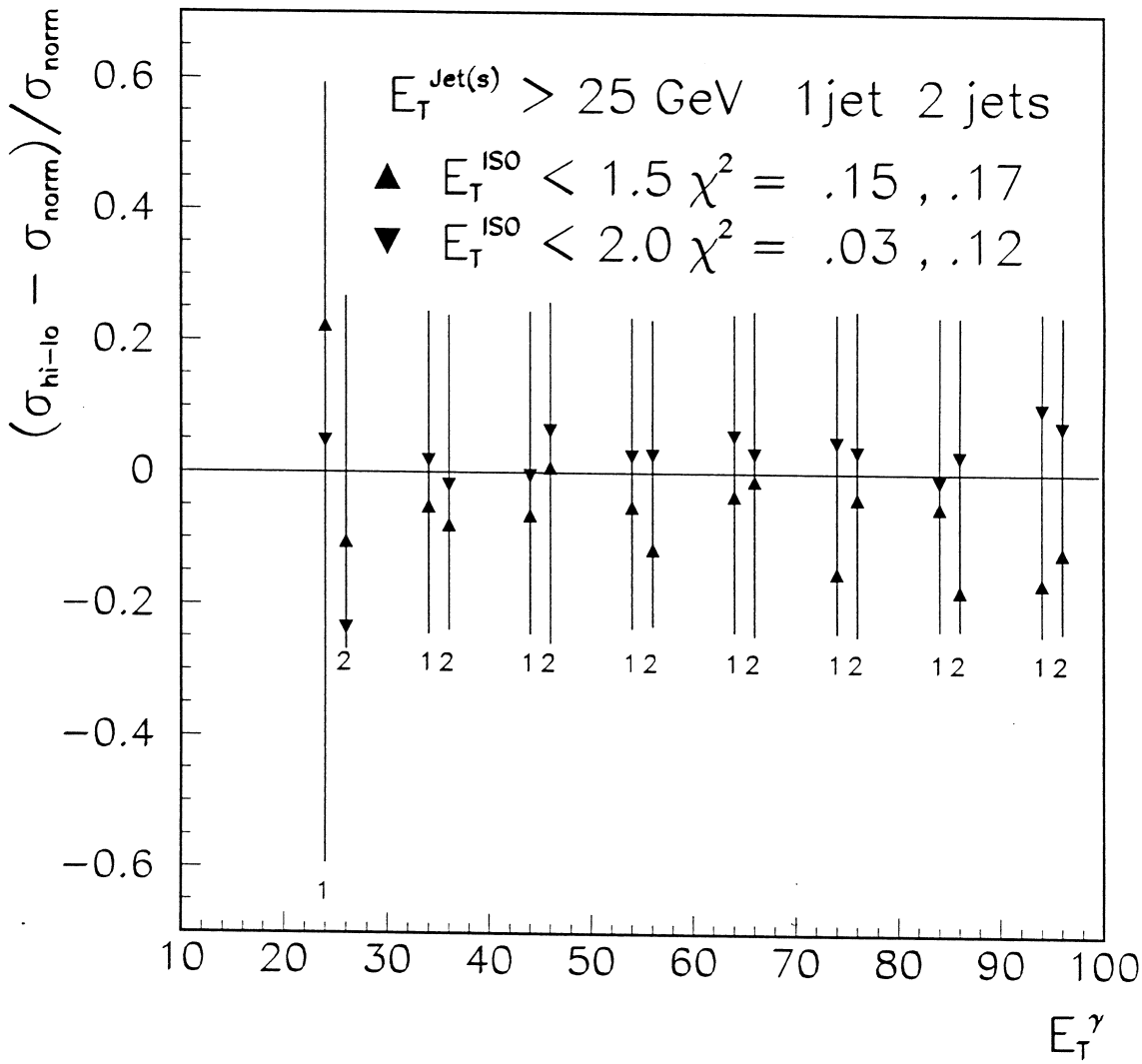

Figure A.3: Dependance of the Cross Sections on the Isolation Cut. The axis represents the cross sections as calculated with the nominal cuts, the up and down arrows show the respective 'tight' and 'loose' cuts. The χ^2 / *d.o.f.* is then shown for each cut, and both the one and two jet cross sections. The error bars show the systematic errors for the nominal cut choice. The numbers underneath each error bar distinguish the one and two jet cases respectively

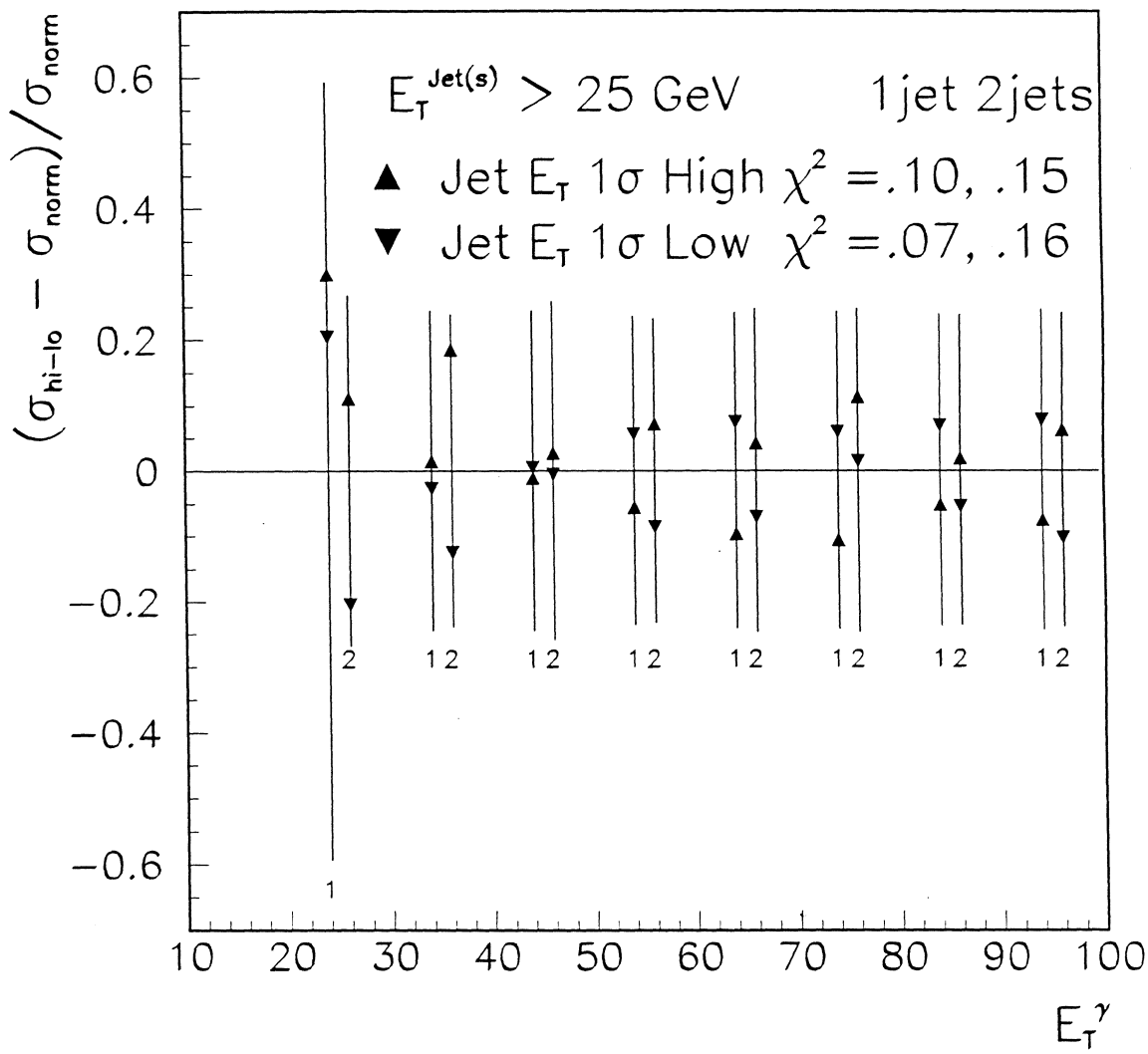

Figure A.4: Dependance of the Cross Sections on the Jet Energy Scale. The axis represents the cross sections as calculated with the nominal jet energy, the up and down arrows show the respective 'high' and 'low' jet energy estimate results. The χ^2 / *d.o.f.* is then shown for each case, for both the one and two jet cross sections. The error bars show the systematic errors for the nominal jet energy choice. The numbers underneath each error bar distinguish the one and two jet cases respectively

APPENDIX B
PLOTS

B.1 Trigger Efficiencies as a Function of E_T^γ

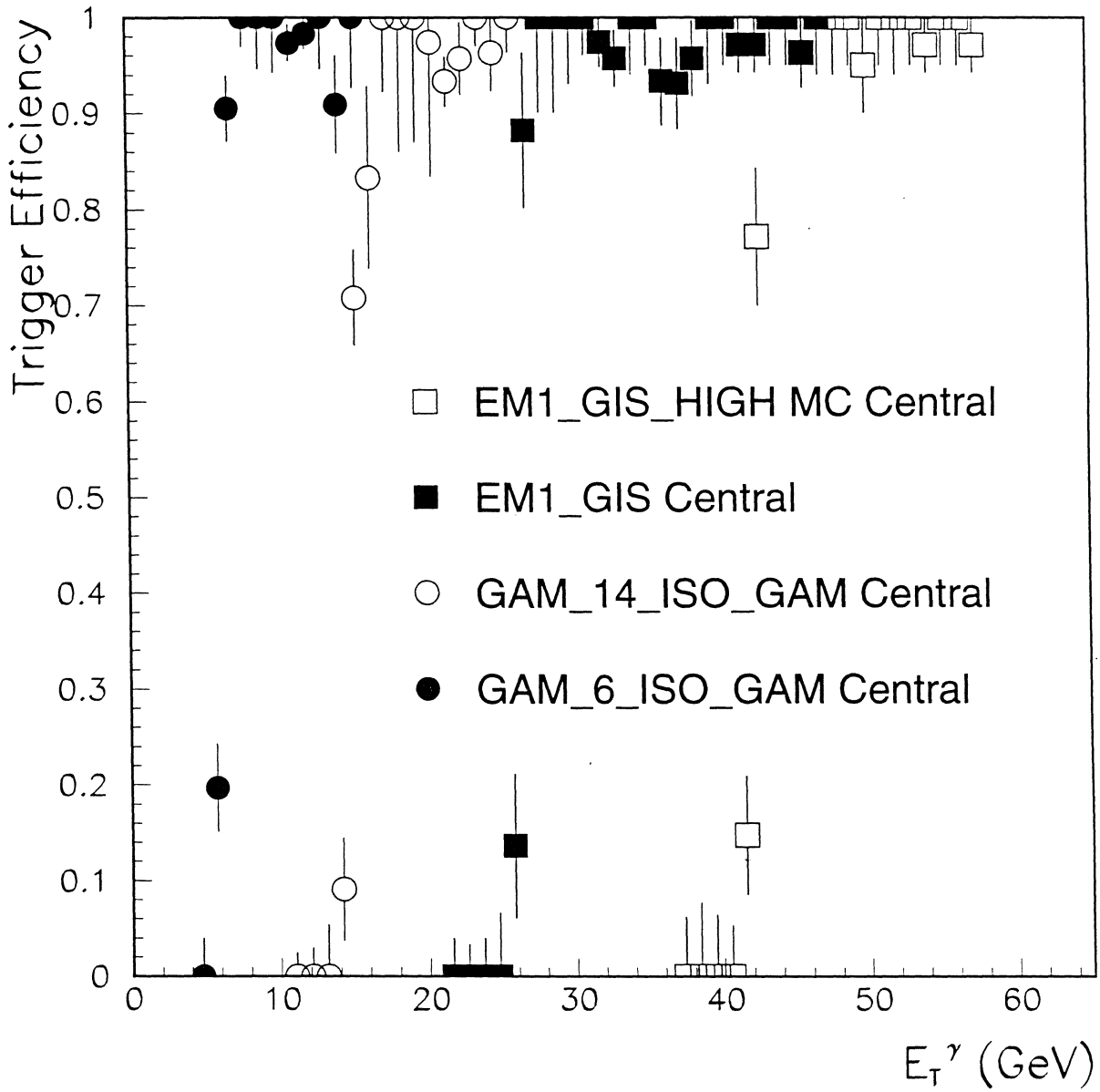

Figure B.1: Turnon of All Triggers. The efficiency of each trigger is plotted with statistical errors as a function of simulated photon E_T.

B.2 Purity Fits

The following plots are the result of the purity calculation for the photon plus one jet case, where the minimum jet E_T was 25 GeV.

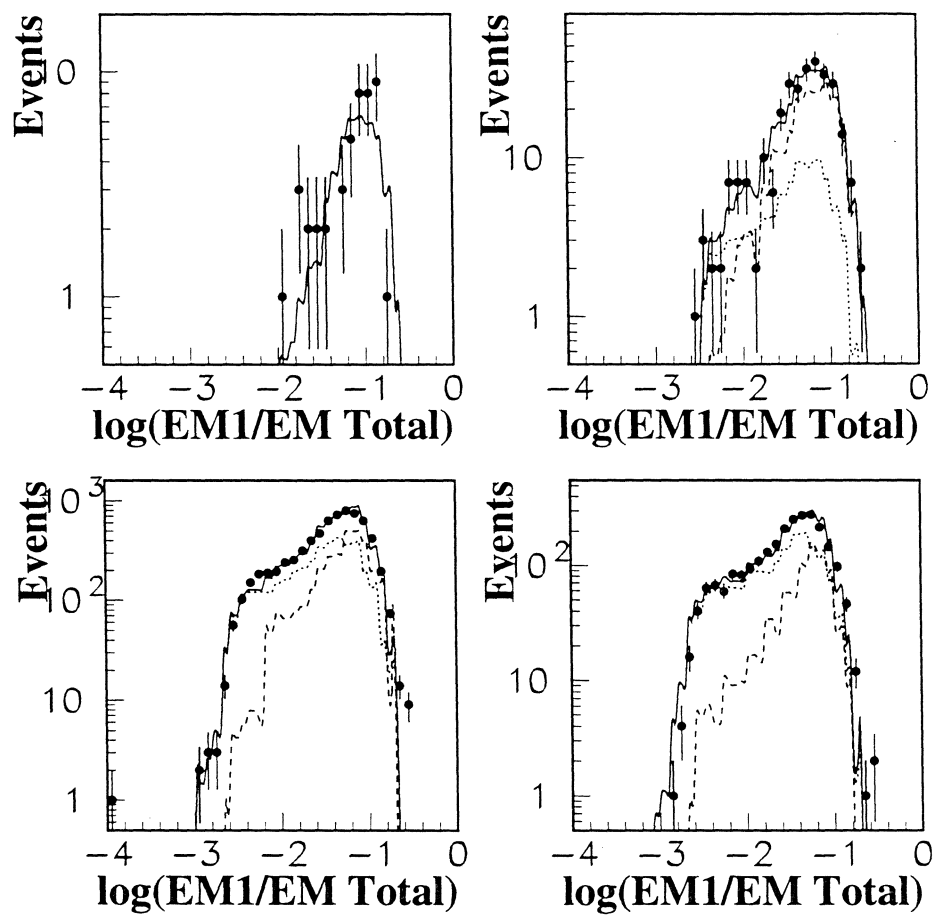

Figure B.2: Fitted Distributions of the Discriminant Variable. Data are shown with statistical errors, the smoothed MC photons and jet distributions are given by the dashed and dotted lines respectively. The fits are given by the solid lines. From left to right and top to bottom, the fits are shown for E_T^γ in the ranges 10-20, 20-30, 30-40, and 40-50 GeV. Data points in the region $\sim$ -.5 that are not well fit by the MC were due to detector effects which were not well modeled by the MC. However, by ignoring these few events in the fit, the resulting purities change by $\sim$.1%, since as expected, the fits are dominated by the low end tails.

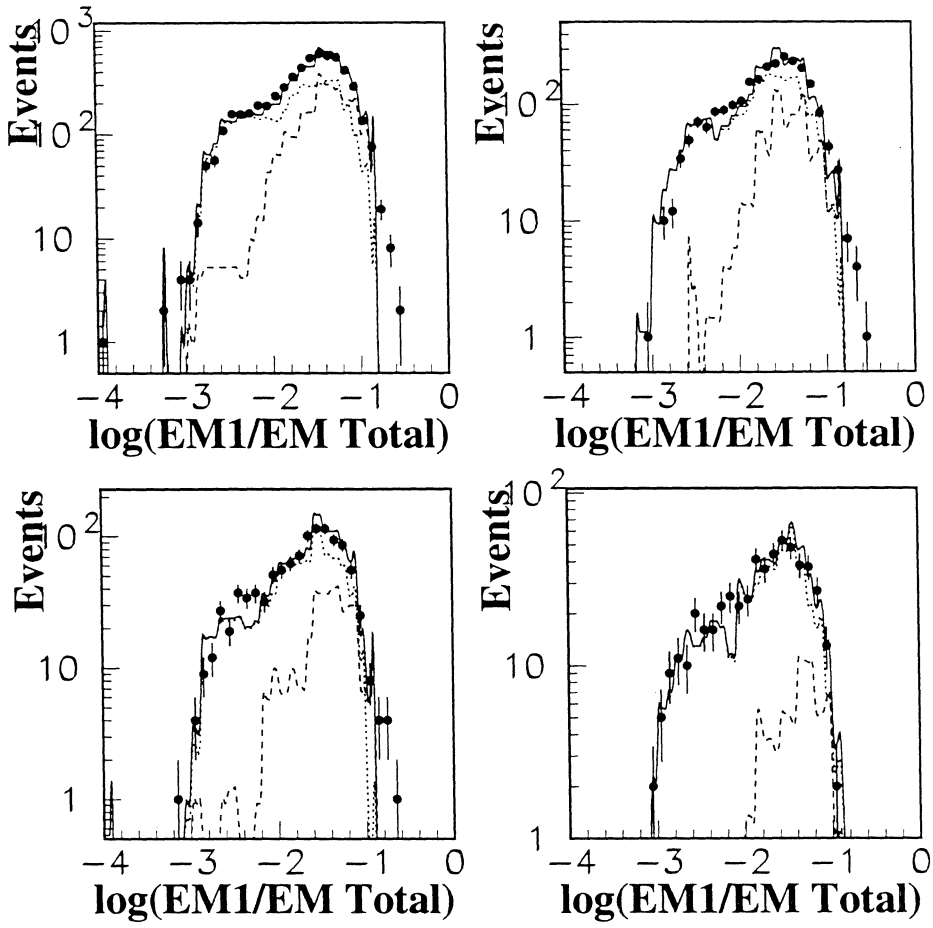

Figure B.3: Fitted Distributions of the Discriminant Variable. Data are shown with statistical errors, the smoothed MC photons and jet distributions are given by the dashed and dotted lines respectively. The fits are given by the solid lines. From left to right and top to bottom, the fits are shown for E_T^γ in the ranges 50-60, 60-70, 70-80, and 80-90 GeV. Data points in the region $\sim$ -.5 that are not well fit were due to detector effects which were not well modeled by the MC. However, by ignoring these few events in the fit, the resulting purities change by $\sim$.1%, since as expected, the fits are dominated by the low end tails.

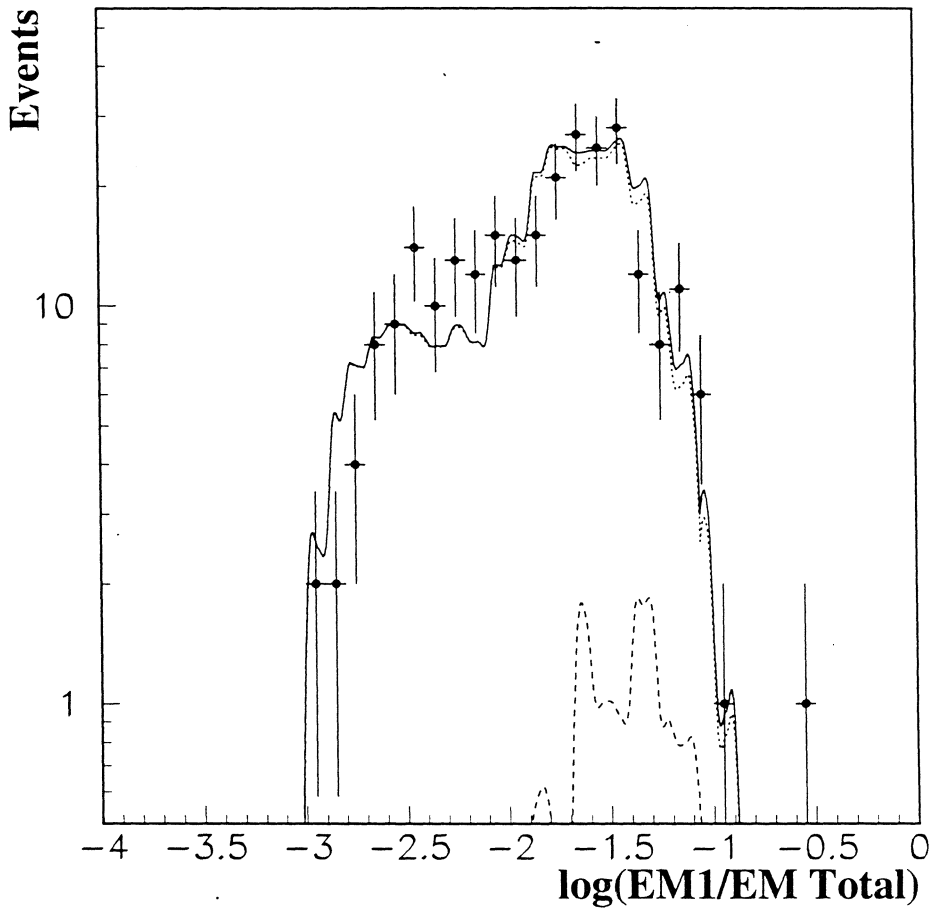

Figure B.4: Fitted Distributions of the Discriminant Variable. Data are shown with statistical errors, the smoothed MC photon and jet distributions are given by the dashed and dotted lines respectively. The fit is given by the solid line. For this figure $90 < E_T^\gamma < 100$ GeV.

BIBLIOGRAPHY

[1] Joseph F. Owens and Wu-Ki Tung, "Parton Distribution Functions of Hadrons" Annu. Rev. Nucl. Part. Sci., **42**, 291 (1992)

[2] M. Diakonou *et al.*, " A Measurement of Direct Photon Production at Large P_T at the CERN ISR", Phys. Lett. **91B**, 296 (1980)

[3] A.L.S. Angelis *et al.*, " Search for Direct Single-Photon Production at Large P_T in Proton-Proton Collisions a $\sqrt{s}$ =62.4 GeV ", Phys. Lett. **94B**, 106 (1980)

[4] H. Baer, J. Ohnemus and J. Owens, "A Calculation of the Direct Photon Plus Jet Cross Section in the Next-to Leading-Logarithm Approximation" Phys. Lett. **B234** 127 (1990)

[5] C. Albajar *et al.*, " Direct Photon Production at the CERN Proton-Antiproton Collider ", Phys. Lett. B **123B**, 367 (1988)

[6] J. Alitti *et al.*, " A Measurement of the Direct Photon Production Cross Section at the CERN $\overline{p}p$ Collider", Phys. Lett. **263B**, 544 (1991)

[7] A. Bernasconi *et al.*, " Direct Photon Production in Proton-Antiproton Interactions at $\sqrt{s}$ = 24.3 GeV ", Phys. Lett. **206**, 163 (1988)

[8] J. Alitti *et al.*, " Measurement of the Gluon Structure Function form Direct Photon Data at the CERN $\overline{p}p$ Collider ", Phys. Lett. **299B**, 174 (1992)

[9] G. Sozzi*et al.*, "Direct Photon Production in $\overline{p}p$ and pp Interactions at $\sqrt{s}$ = 24.3 GeV ", Phys. Lett. **B317** 243 (1993)

[10] G. Alverson, " Direct Photon Production at High P_T in $\pi^- Be$ and pBe Collisions at 500 GeV/c ", Phys. Rev. Lett. **68** 2584 (1992)

[11] F. Abe *et al.*, " Measurement of the Isolated Prompt Photon Cross Section in $\overline{p}p$ Collisions at $\sqrt{s} = 1.8$ TeV ", Phys. Rev. Lett. **68**, 2734 (1992)

[12] F. Abe *et al.*, " Precision Measurement of the Prompt Photon Cross Section in $\overline{p}p$ Collisions at $\sqrt{s} = 1.8$ TeV", Phys. Rev. Lett. **73**, 2662 (1994)

[13] F. Abe *et al.*, " Prompt Photon Cross Section Measurement in $\overline{p}p$ Collisions at $\sqrt{s} = 1.8$ TeV ", Phys. Rev. **D48**, 2998 (1993)

[14] F. Abe *et al.*, " Center-of-Mass Angular Distribution of Prompt Photons Produced in $p\overline{p}$ Collisions at $\sqrt{s} = 1.8$ TeV ", Phys. Rev. Lett. **71**, 679 (1993)

[15] P.A. Maas "Properties of Events Containing a Photon and Several Jets Seen in $\overline{p}p$ Collisions at $\sqrt{s}$ =1.8 TeV " unpublished dissertation, Univ. of Wisconsin - Madison (1993)

[16] S. Abachi *et al.*, " Isolated Photon Cross Section in the Central and Forward Rapidity Regions in $p\overline{p}$ collisions at $\sqrt{s} = 1.8$ TeV ", Phys. Rev. Lett. **77**, 5011 (1996)

[17] P. Rubinov, " The Center-of-Mass Angular Distribution of Direct Photon Production at $\sqrt{s}$ =1.8 TeV Observed With the DØ Detector ", unpublished dissertation, S.U.N.Y. at Stony Brook, (1995)

[18] R. Madden, " Direct Photon Production and Search for Excited Quarks with the DØ Detector ", unpublished dissertation, Florida State U. , (1995)

[19] U. Baur, I. Hinchliffe, and D. Zeppenfeld, " Excited Quark Production at Hadron Colliders ", Int. J. Mod. Phys. A , v2 n4, 1285 (1987)

[20] S. Abachi *et al.*, "The DØ Detector", Nucl. Instr. And Methods **A338**, 185 (1994)

[21] H. Melanson, "Electron Efficiency Studies ", unpublished DØnote (1996)

[22] B. Lauer, Private communication

[23] S. Abachi *et al.*, "Beam Test of the DØ Uranium Liquid Argon End Calorimeters", Nucl. Inst. Meth. **A324**, 53, (1993)

[24] M. Abloins *et al.*, "Hadron and Electron response if Uranium Liquid Argon Calorimeter Modules for the DØ Detector", Nucl. Inst. Meth. **A280**, 36, (1989)

[25] F. Abe *et al.*, " Measurement of Small Angle $\overline{p}p$ Elastic Scattering at $\sqrt{s} = 546$ and 1800 GeV ", Fermilab-Pub-93/232-E (1993)

[26] F. Abe *et al.*, " Measurement of $\overline{p}p$ Single Diffractive Dissociation at $\sqrt{s} = 546$ and 1800 GeV", Fermilab-Pub-93/233-E (1993)

[27] F. Abe *et al.*, " Measurement of the $\overline{p}p$ Total Cross Section at $\sqrt{s} = 546$ and 1800 GeV", Fermilab-Pub-93/234

[28] N. Amos *et al.*, " A Luminosity-Independent Measurement of the $\overline{p}p$ Total Cross Section at $\sqrt{s} = 1.8$ TeV ", Phys. Lett. **243B**, 158 (1990)

[29] J. McKinley, J. Linnemann "L2_EM.DOC", internal DØ publication (1993)

[30] M. Narain for the DØ Collaboration, "Electron Identification in the DØ Detector", FERMILAB-Conf-93/054-E, unpublished (1993)

[31] R. Englemann *et al.*, Nucl. Instr. Meth. **216**, 45 (1983)

[32] R. Hirosky, " A Data-based Estimate of Jet Reconstruction Efficiencies ", DØNOTE 2369 (1994)

[33] M. Bhattacharjee *et al.* "Efficiencies of the Standard Jet Cuts for Cone Sizes: 0.3,0.5,0.7 ", DØNOTE 2197

[34] S. Linn, " The Photon Purity in the Central Rapidity Region", DØNOTE2326 (1995)

[35] T. Sjöstrand, Comp. Phys. Comm., **82**, 74, (1994)

[36] F. Carminati et al., "GEANT Users Guide", CERN Program Library, (1991)

[37] T. Sjöstrand, Phys. Lett. **157B**, 321 (1985)

[38] M, Bengtsson & T. Sjöstrand, Phys. Lett. **185B** p435 (1987) and M, Bengtsson & T. Sjöstrand, Nucl. Phys **B289**, 810 (1987)

[39] B. Andersson, G. Gustafson, G. Ingleman, and T. Sjöstrand, Phys. Rev. **97**, 31 (1983)

[40] J.D. Jackson, "Classical Electrodynamics", Wesley & Sons , 715 (1975)

[41] H. Baer, J. Ohnemus and J. Owens, "Next-to-Leading-Logarithm Calculation of Direct Photon Production", Phys. Rev. **D42**, 61 (1990)

[42] T. Joffe-Minor, unpublished DØnote, (1996)

[43] H. Baer and M. Reno, " Multiple Parton Emission Effects in Next-to-Leading Order Direct Photon Production ", Phys. Rev. D **D54**, 2017 (1996)

Christopher D. Shaffer graduated from Hope College in Holland, Michigan in 1990 with majors in Mathematics and Physics. He then attended Florida State University where he joined the DØ experiment at the Fermi National Accelerator Laboratory. He obtained his masters degree in 1993 and doctorate in 1997. A list of 30 publications which he co-authored follows.

"Search for Anomalous W W and W Z Production in p anti-p Collisions at $\sqrt{s}$ = 1.8-TeV " Phys. Rev. Lett. **77** (1996) 3303-3308

"Measurement of the W Boson Mass" Phys. Rev. Lett. **77** 3309-3314 (1996)

"Search for Additional Neutral gauge Bosons" Phys. Lett. **B385** 471-478 (1996)

"Search for a Fourth Generation Charge -1/3 Quark via Flavor Changing Neutral Current Decay" Submitted to Phys. Rev. Lett.

"Limits on Anomalous W W Gamma Couplings from p anti-p $\rightarrow$ W Gamma + X Events at $\sqrt{s}$ = 1.8-TeV" Submitted to Phys. Rev. Lett.

"Search for Diphoton Events With Large Missing Transverse Energy in p - anti-p Collisions at $\sqrt{s}$ = 1.8-TeV" Phys. Rev. Lett. **78** 2070-2074 (1997)

"Search for Top Squark Pair Production in the Dielectron Channel" Submitted to Phys. Lett. B

"Direct Measurement of the Top quark Mass" Submitted to Phys. Rev. Lett.

"The Isolated Photon Cross Section in the Central and Forward Rapidity Regions in p anti-p Collisions at $\sqrt{s}$ = 1.8-TeV" Phys. Rev. Lett. **77** 5011-5015 (1996)

"The Azimuthal Decorrelation of Jets Widely Separated in Rapidity" Phys. Rev. Lett. **77** 5011-5015 (1996)

"J / Psi Production in p anti-p Collisions at $\sqrt{s}$ = 1.8-TV" Phys. Lett. **B370** 239-248 (1996)

"Search for Light Top Squarks in p anti-p Collisions at $\sqrt{s}$ = 1.8-TeV" Phys. Rev. Lett. **76** 2222-2227 (1996)

"Search for Righthanded W Bosons and Heavy W-prime in p anti-p Collisions at $\sqrt{s}$ = 1.8-TeV" Phys. Rev. Lett. **76** 3271-3276 (1996)

"Search for Supersymmetric W(1) Z(2) Production via Trilepton Final States in p anti-p Collisions at $\sqrt{s}$ = 1.8-TeV" Phys. Rev. Lett. **76** 2228-2233 (1996)

"Search for Heavy W Boson in 1.8-TeV p anti-p Collisions" Phys. Lett. **B358** 405-411 (1995)

"Jet Production via Strongly Interacting Color Singlet Exchange in p anti-p Collisions" Phys. Rev. Lett. **76** 734-739 (1996)

"Studies of Topological Distributions of Inclusive the Three and Four Jet Events in anti-p p Collisions at $\sqrt{s}$ = 1800-GEV with the DØ Detector" Phys. Rev. **D53** 6000-6016 (1996)

"Top Quark Search with the DØ 1992 - 1993 Data Sample" Phys. Rev. **D52** 4877-4919 (1995)

"Limits on the Anomalous Z Z Gamma and Z gamma Gamma Couplings in p anti-p Collisions at $\sqrt{s}$ = 1.8-TeV" Phys. Rev. Lett. **75** 1028-1033 (1995)

"Transverse Energy Distributions Within Jets in p anti-p Collisions at $\sqrt{s}$ = 1.8-TeV" Phys. Lett. **B357** 500-508 (1995)

"Second Generation Leptoquark Search in p anti-p Collisions at $\sqrt{s}$ = 1.8-TeV" Phys. Rev. Lett. **75** 3618-3623 (1995)

"W and Z Boson Production in p anti-p Collisions at $\sqrt{s}$ = 1.8-TeV" Phys. Rev. Lett. **75** 1456-1461 (1995)

"Search for Squarks and Gluinos in p anti-p Collisions at $\sqrt{s}$ =1.8-TeV" Phys. Rev. Lett. **75** 618-623 (1995)

"Measurement of the W W Gamma Gauge Boson Couplings in p anti-p Collisions at $\sqrt{s}$ = 1.8-TeV" Phys. Rev. Lett. **75** 1034-1039 (1995)

"A Study of the Strong Coupling Constant Using W + Jets Processes" Phys. Rev. Lett. **75** 3226-3231 (1995)

"Measurement of the Z Z Gamma and Z Gamma Gamma Couplings in p anti-p Collisions at $\sqrt{s}$ = 1.8-TeV" Phys. Rev. Lett. **75** 1028 (1995)

"Search for W Boson Pair Production in p anti-p Collisions at $\sqrt{s}$ = 1.8-TeV" Phys. Rev. Lett. **75** 1023-1027 (1995)

"Observation of the Top Quark" Phys. Rev. Lett. **74** 2632-2637 (1995)

"Inclusive mu and b Quark Production Cross Sections in p anti-p Collisions at $\sqrt{s}$ = 1.8-TeV" Phys. Rev. Lett. **74** 3548-3552 (1995)

"Search for High Mass Top Quark Production in p anti-p Collisions at $\sqrt{s}$ = 1.8-TeV" Phys. Rev. Lett. **74** 2422-2426 (1995)